UNCLASSIFIED

AD NUMBER

ADB204824

NEW LIMITATION CHANGE

TO

Approved for public release, distribution unlimited

FROM

Distribution authorized to DoD only; Specific Authority/Proprietary Info.; 15 Nov 95. Other requests shall be referred to Commander, U.S. Army Medical Research and Materiel Command, Attn: MCMR-RMI-S, Ft. Detrick, MD 21702-5012.

AUTHORITY

U.S. Army Medical Research and Materiel Command ltr., dtd January 21, 2000.

THIS PAGE IS UNCLASSIFIED

AD

CONTRACT NUMBER: DAMD17-95-C-5055

TITLE: Non-Invasive NIR Sensor for Quantification of Deep Tissue Oxygenation

PRINCIPAL INVESTIGATOR: H. Sang Lee, Ph.D.

CONTRACTING ORGANIZATION: Science and Engineering Services Inc.
Burtonsville, Maryland 20866

REPORT DATE: October 1995

TYPE OF REPORT: Final, Phase I

PREPARED FOR: U.S. Army Medical Research and Materiel Command
Fort Detrick, Maryland 21702-5012

PROPRIETARY INFORMATION

DISTRIBUTION STATEMENT: Distribution authorized to DoD Components only, Specific Authority. Other requests shall be referred to the Commander, U.S. Army Medical Research and Materiel Command, ATTN: MCMR-RMI-S, Fort Detrick, MD 21702-5012

REPORT DOCUMENTATION PAGE

Form Approved
OMB No. 0704-0188

1. AGENCY USE ONLY *(Leave blank)*

2. REPORT DATE
October 1995

3. REPORT TYPE AND DATES COVERED
Final, Phase I 15 Mar 95 - 14 Sep 95

4. TITLE AND SUBTITLE
Non-Invasive NIR Sensor for Quantification of Deep Tissue Oxygenation

5. FUNDING NUMBERS
DAMD17-95-C-5055

6. AUTHOR(S)
H. Sang Lee, Ph.D.

7. PERFORMING ORGANIZATION NAME(S) AND ADDRESS(ES)
Science and Engineering Services, Inc.
Burtonsville, Maryland 20866

8. PERFORMING ORGANIZATION REPORT NUMBER
AR01-001

9. SPONSORING/MONITORING AGENCY NAME(S) AND ADDRESS(ES)
U.S. Army Medical Research and Materiel Command
Fort Detrick, Maryland 21702-5012

10. SPONSORING/MONITORING AGENCY REPORT NUMBER

11. SUPPLEMENTARY NOTES
Proprietary information is contained from page 8 to page 51. Protection of the information is needed.

PROPRIETARY INFORMATION

12a. DISTRIBUTION/AVAILABILITY STATEMENT
Distribution authorized to DoD Components only, Specific Authority. Other requests shall be referred to Commander, U.S. Army Medical Research and Materiel Command, ATTN: MCMR-RMI-S, Fort Detrick, Maryland 21702-5012

12b. DISTRIBUTION CODE

13. ABSTRACT *(Maximum 200 words)*

A breadboard NIR sensor system was developed for the purpose of accurate quantification of deep tissue oxygenation based on a novel Pseudo-Random Modulation/Resolution Enhancement Technique (PRM/RET). It consists of a CW modulated diode laser coupled with optical fiber, a detector, and a sampling oscilloscope. Temporal resolution of 40 psec with a 200 MHZ PRM system is demonstrated, which is 100 fold improvement over the conventional limit of the PRM technique. Experiments using a homogeneous phantom demonstrate a measurement accuracy of 0.001 cm^{-1} for absorption coefficient μ_a, and 0.07 cm^{-1} for scattering coefficient μ_s. This accuracy provides the detectability of a few percent oxygenation change in tissue blood. The differential measurement using two NIR wavelengths demonstrates the utility for absolute qunatification of oxygenation. A simple method was developed to perform sensitive and self-consistent absorption and scattering coefficients measurement, suitable for battle field applications. A remarkable depth resolution was demonstrated in an absorber depth measurement experiment, suggesting the direct applicability of the sensor system to clinical deep tissue diagnosis. Design for Phase II prototype system which is portable, low cost, and low power consumption is presented.

14. SUBJECT TERMS

PRM/RET	NIRS	Deep Tissue
Oxygenation	Diagnosis	Cost-Effective
Battlefield	Critically-ill-patient	

15. NUMBER OF PAGES
65

16. PRICE CODE

17. SECURITY CLASSIFICATION OF REPORT	18. SECURITY CLASSIFICATION OF THIS PAGE	19. SECURITY CLASSIFICATION OF ABSTRACT	20. LIMITATION OF ABSTRACT
Unclassified	Unclassified	Unclassified	Limited

GENERAL INSTRUCTIONS FOR COMPLETING SF 298

The Report Documentation Page (RDP) is used in announcing and cataloging reports. It is important that this information be consistent with the rest of the report, particularly the cover and title page. Instructions for filling in each block of the form follow. It is important to *stay within the lines* to meet *optical scanning requirements*.

Block 1. Agency Use Only (*Leave blank*).

Block 2. Report Date. Full publication date including day, month, and year, if available (e.g. 1 Jan 88). Must cite at least the year.

Block 3. Type of Report and Dates Covered. State whether report is interim, final, etc. If applicable, enter inclusive report dates (e.g. 10 Jun 87 - 30 Jun 88).

Block 4. Title and Subtitle. A title is taken from the part of the report that provides the most meaningful and complete information. When a report is prepared in more than one volume, repeat the primary title, add volume number, and include subtitle for the specific volume. On classified documents enter the title classification in parentheses.

Block 5. Funding Numbers. To include contract and grant numbers; may include program element number(s), project number(s), task number(s), and work unit number(s). Use the following labels:

C - Contract
G - Grant
PE - Program Element
PR - Project
TA - Task
WU - Work Unit Accession No.

Block 6. Author(s). Name(s) of person(s) responsible for writing the report, performing the research, or credited with the content of the report. If editor or compiler, this should follow the name(s).

Block 7. Performing Organization Name(s) and Address(es). Self-explanatory.

Block 8. Performing Organization Report Number. Enter the unique alphanumeric report number(s) assigned by the organization performing the report.

Block 9. Sponsoring/Monitoring Agency Name(s) and Address(es). Self-explanatory.

Block 10. Sponsoring/Monitoring Agency Report Number. *(If known)*

Block 11. Supplementary Notes. Enter information not included elsewhere such as: Prepared in cooperation with...; Trans. of...; To be published in.... When a report is revised, include a statement whether the new report supersedes or supplements the older report.

Block 12a. Distribution/Availability Statement. Denotes public availability or limitations. Cite any availability to the public. Enter additional limitations or special markings in all capitals (e.g. NOFORN, REL, ITAR).

DOD - See DoDD 5230.24, "Distribution Statements on Technical Documents."
DOE - See authorities.
NASA - See Handbook NHB 2200.2.
NTIS - Leave blank.

Block 12b. Distribution Code.

DOD - Leave blank.
DOE - Enter DOE distribution categories from the Standard Distribution for Unclassified Scientific and Technical Reports.
NASA - Leave blank.
NTIS - Leave blank.

Block 13. Abstract. Include a brief (*Maximum 200 words*) factual summary of the most significant information contained in the report.

Block 14. Subject Terms. Keywords or phrases identifying major subjects in the report.

Block 15. Number of Pages. Enter the total number of pages.

Block 16. Price Code. Enter appropriate price code (*NTIS only*).

Blocks 17. - 19. Security Classifications. Self-explanatory. Enter U.S. Security Classification in accordance with U.S. Security Regulations (i.e., UNCLASSIFIED). If form contains classified information, stamp classification on the top and bottom of the page.

Block 20. Limitation of Abstract. This block must be completed to assign a limitation to the abstract. Enter either UL (unlimited) or SAR (same as report). An entry in this block is necessary if the abstract is to be limited. If blank, the abstract is assumed to be unlimited.

*U.S.GPO:1991-0-299-935

FOREWORD

Opinions, interpretations, conclusions and recommendations are those of the author and are not necessarily endorsed by the US Army.

H.S.L Where copyrighted material is quoted, permission has been obtained to use such material.

H.S.L Where material from documents designated for limited distribution is quoted, permission has been obtained to use the material.

H.S.L Citations of commercial organizations and trade names in this report do not constitute an official Department of Army endorsement or approval of the products or services of these organizations.

____ In conducting research using animals, the investigator(s) adhered to the "Guide for the Care and Use of Laboratory Animals," prepared by the Committee on Care and Use of Laboratory Animals of the Institute of Laboratory Resources, National Research Council (NIH Publication No. 86-23, Revised 1985).

____ For the protection of human subjects, the investigator(s) adhered to policies of applicable Federal Law 45 CFR 46.

____ In conducting research utilizing recombinant DNA technology, the investigator(s) adhered to current guidelines promulgated by the National Institutes of Health.

____ In the conduct of research utilizing recombinant DNA, the investigator(s) adhered to the NIH Guidelines for Research Involving Recombinant DNA Molecules.

H.S.L In the conduct of research involving hazardous organisms, the investigator(s) adhered to the CDC-NIH Guide for Biosafety in Microbiological and Biomedical Laboratories.

Accesion For
NTIS CRA&I ☐
DTIC TAB ☑
Unannounced ☐
Justification ....
By ....
Distribution /
Availability Codes

Dist	Avail and / or Special
E-4	

10/6/95
PI - Signature Date

Table of Contents

1. Introduction

1.1. Significance of PRM Measurement of Percent Hemoglobin Saturation

Deep Tissue Oxygen Exchange Events in Relation to Isolated Organ Function

Delivery of oxygen to tissue can be assessed by several different types of physiologic measurements such as blood flow measurements, blood velocity measurements, blood oxygen extraction measurements, and/or tissue oxygenation measurements [Ferrari, et al., 1992]. Oxidative metabolism is important because it is the fundamental biochemical process that tissues use to support organ specific work. Thus any increase in physiologic work is matched to an increase in metabolic requirements that support this work. For example, increased brain activity, increased cardiac pumping, muscle contraction, kidney or hepatic function all require increases in energy supplied and consumed that will proportionately support these increased activities. Conversely, the monitoring of vital organ function and the specific tasks these functions serve can be achieved by monitoring changes in organ specific deep tissue hemoglobin saturation.

A number of physiologic parameters describe the circulatory mechanics of blood flow and control tissue oxygenation. The sequence of events is: 1) delivery of oxygen to the tissue by red blood cells saturated with oxygen, 2) the dispersion of this blood into the tissue by a capillary network and 3) the off loading of oxygen into tissue where myoglobin and mitochondria accept it and make oxygen available for redox reactions important to the body's function. Blood flow and organ oxygen extraction have a particularly close physiologic relationship in all biologic systems. Thus the greater the blood flow to a specific organ the greater the total amount of oxygen delivered. Conversely the greater the amount of tissue oxygen consumption the lower that capillary hemoglobin saturation falls. This is reflected in the venous saturation of hemoglobin or SvO_2. Accurate accounting for isolated organ oxygen uptake requires a knowledge of organ blood flow and organ specific fractional oxygen extraction. When organ blood flow is constant, changes in the hemoglobin saturation of exiting blood also reflect changes in organ specific oxygen metabolism.

Several deep organs have the potential to allow for assessment of this association between oxygen metabolism and organ function. These include the brain, heart, kidney, muscle and intestinal/hepatic systems. Brain, heart, and kidney share the circulatory property of autoregulation that allows for a homeostatic constancy of organ blood flow under a wide set of conditions. In contrast the musculoskeletal, intestinal, hepatic, and skin systems are more sensitive to both neural and perfusion pressure changes that lead to a wider range of both tissue blood flows and associated oxygen extraction states. By monitoring normal and abnormal functions, the range of organ specific information may be particularly helpful in defining the concurrence of normal organ function in all these systems or the presence of specific singular organ dysfunction.

The physiologic challenge of obtaining noninvasive oxygen metabolism is in many ways similar for each of these organ systems. All have overlying tissue including bone, musculoskeletal tissue, and frequently fatty tissue that may provide for optical and biochemical interference in the process of accurately assessing deep tissue oxygenation. To date the best available noninvasive deep tissue oxygen measurements have been made from brain [Wyatt, et al., 1990; Mancini, et al., 1994; Chance, et al., 1988; Ferrari, et al., 1989]. The earlier work at Hopkins in quantitating cerebral hemoglobin saturation of brain tissue (cerebral SvO_2) is among the first in the reflectance mode of these demonstrations [Ferrari, et al., 1989]. Since that time a significant number of physiologic illustrations of surface tissue oxygenation events have been developed.

Normal and Abnormal Deep Tissue Oxygenation Events

Normal deep tissue events that are noted to produce changes in organ blood flow of tissue hemoglobin saturation would potentially be measurable with PRM/RET optical sensors. These include flow dependent changes in hepatic oxygenation during digestion system activation [Nowiki, et al., 1983; Chou 1983], or hypothermia induced changes in skin blood flow. Within the brain, stimulus dependent activation of specific afferent and efferent brain areas [Vilringer, et al., 1994] and/or sleep/wake cycle differences in brain oxygenation are known to occur. Similarly physical activity may provoke different patterns of change in deep tissue oxygenation depending upon the task, a differential activation of cardiac, brain, skin, muscle, and other organs may occur.

Under situations of stress or potential injury, other changes in deep tissue oxygenation are known to occur and may provide substantial specificity if a large number of organs can be assessed accurately. For example, failure of either the mechanical aspects of ventilation or failure of gas exchange because of hypoxia will produce a rapid global decrease in hemoglobin saturation followed by autoregulatory blood flow increases in brain, cardiac, and renal tissues. Skin and liver demonstrate a substantially greater drop in oxygenation than brain, heart, and kidneys [Jensen, et al., 1987]. Conversely, circulatory failure from hemorrhagic shock produces impaired oxygen consumption with a normal arterial oxygen saturation but expanding extraction fraction. In situations where injury is focal within a particular organ system, increased heterogeneity of tissue oxygenation occurs. This is particularly true for infarctions and direct mechanical trauma which both impede circulation to regions of an organ. Thus, for infarction or trauma tissue hemoglobin saturation signals would demonstrate a wider range of oxygen extraction than in the non-injured situation [Buchweitz-Milton and Weiss, 1987]. Similarly tissue injury commonly involves hemorrhage with the loss of blood to either local tissue areas or outside the body itself. Of the local areas the liver is particularly vulnerable [Bulkley, et al., 1986; Flynn, et al., 1994]. In both situations unique patterns of deep tissue oxygenation signals may occur. Where hemoglobin in lost from the body and repletion of circulating fluids occurs with plasma, a decrease in the overall hemoglobin signal is noted [Ferrari, et al., 1990]. Where local accumulation of blood clot occurs and an optical sensor is in the immediate environment, a remarkable increase in optical density occurs [Gopinath, et al., 1993]. Alternatively tissue damage in the musculoskeletal system is often associated with the release of myoglobin into the circulation. Were this to occur myoglobin specific absorption might appear in organs such as skin or brain that do not ordinarily contain myoglobin. Thus fully implemented an organ specific multi-sensor system would allow for the fusion of organ specific oxygenation information into a physiologic or pathophysiologic signature of normal and abnormal events. With properly implemented algorithms this sensor information could be compressed and telemetered to remote sites for immediate evaluation of specific elements of human performance.

Advantages of PRM/RET Sensor Methodology for Deep Tissue Monitoring

Deep tissue assessments generally require measurements from organ sites that are 3 or more cm below the skin surface. The available technologies that allow for either reflectance or transmission spectroscopy at these depths require time sensitive measurements of ballistic photons. PRM/RET technology allows for a low energy input and easily automated paradigm to be used. Both characteristics are substantial enhancements over the original time resolved spectroscopy methods. While PRM/RET techniques assess tissue-light interaction in the nanosecond time domain producing temporal dispersion patterns that allow for quantitation of μ_a and μ_s, the absence of picosecond resolution most likely represents a significant advantage in two clinical areas. First the PRM sequence allows for lower energy inputs that are consistent with multiple rapid sequential measurements that can be averaged producing physiologic signals in the one hertz time domain. Second despite the somewhat slower time performance of PRM/RET technology in comparison to absolute time of flight measurements, this technology and the averaging of sensor signals will allow for averaging paradigms to eliminate subject motion that might otherwise distort the signal.

1.2. Summary of Phase I Results

A breadboard NIR sensor system was developed for the purpose of accurate quantification of deep tissue oxygenation based on a novel Pseudo-Random Modulation/Resolution Enhancement Technique (PRM/RET). The breadboard system consists of a CW modulated diode laser with optical fiber light delivery, a detector, and a sampling oscilloscope. It was used for time resolved spectroscopic (TRS) measurements of photon migration in a phantom model closely resembling a soft tissue.

Analysis of the data from this measurement clearly demonstrates the unique capability of the PRM/RET sensor for accurate, noninvasive measurement of the optical parameters of the phantom. The accuracy demonstrated provides the detectability of a few percent change in oxygenation of tissue blood. A simple method of analyzing the PRM data was developed based on the waveform moment analysis. Test of this method using a phantom demonstrated a very high sensitivity of the first moment to the phantom absorption coefficient. The differential measurement using two NIR wavelengths clearly demonstrates the utility for absolute qunatification of the oxygenation in addition to the total hemoglobin measurement. The breadboard sensor was further applied to verify the deep penetration capability of the PRM measurement, by measuring the depth information of a strongly absorbing layer in a dense scattering medium. A remarkable depth resolution of the breadboard sensor was demonstrated in this experiment suggesting the direct applicability of PRM/RET sensor for clinical deep tissue diagnosis.

A brief list of the tasks we have successfully performed and the novel features of the PRM/RET sensor is as following.

- Verification of PRM/RET technique - The feasibility experiment demonstrated a 100 fold improvement of the temporal resolution using PRM/RET technique over the conventional limit of the PRM technique, providing 40 psec resolution with a 200 MHz PRM system. This resolution was directly applied for the accurate temporal measurement of the deep tissue phantom response function allowing a high accuracy measurement of the phantom optical parameters.

- Quantitative measurement of tissue optical parameters - The breadboard system and simple analysis algorithm demonstrates a measurement accuracy of 0.001 cm^{-1} for absorption coefficient, μ_a, and 0.07 cm^{-1} for scattering coefficient, μ_s, of a homogeneous phantom closely resembling the soft tissue. This measurement accuracy is equivalent to a detectability of 1-2% variation of hemoglobin oxygenation, which is far better than any published results of non-invasive measurements. With an anticipated performance improvement of the prototype sensor, better than 1% accuracy will be obtained.

- Simultaneous differential measurement using common signal path - The unique orthogonal property of the PRM codes with different lengths allows a simultaneous differential measurement for multiple wavelengths using the common signal path from the transmitter optics to the digitizer. The differential measurement using two NIR wavelengths will provide the capability for accurate quantification of the hemoglobin oxygenation and total concentration in deep tissues.

- Large penetration depth with a high S/N - The breadboard system demonstrates penetration depth of over 8 cm in soft tissue with a S/N ratio of >20. Based on the design features, the next prototype will provide an even larger penetration depth with higher S/N ratio, with 1 second signal averaging. Neither the phase modulation spectroscopy (PMS) [Sevick et al, 1991] or a conventional TRS system provides this level of sensitivity in an economic manner.

- Detection and localization of heterogeneity - Detection of strong absorption layer resembling heterogeneous blood concentration was demonstrated clearly in a simulation experiment using the breadboard system. The location of the layer was distinguished up to an 8 cm depth into the scattering medium resembling the soft tissue. Further improvement in resolution and penetration depth is expected with the prototype system.

- Compatibility with other diagnostic instrument for simultaneous operation - The unique noise and bias filtering capability will allow the sensor to operate in a noisy (both for optical and electrical) environment. Remote accessibility using fiber optics enables real time applications in surgical operations or other diagnostic processes.

- Continuous measurement with higher than 1 Hz updating rate - The unique signal processing technique of PRM/RET provides a high throughput signal with low transmitter power and allows a high data acquisition rate of over 1 Hz in the baseline configuration.

- Robust performance of a cost effective portable sensor package - A turnkey system continuously operational over a long period (more than several years) without maintenance requirements will be characteristic of the fully developed clinical system. The cost of the system is anticipated at no more than $20K. This system will be portable with less than 10 liter volume and lower than 50 Watt power consumption. No other TRS instrument offers such a benefit.

2. Phase I Objectives

As a reference to the Phase I results, we include the Phase I objectives below verbatim from the Phase I proposal:

This proposal is to develop a cost effective and reliable NIRS sensor for accurate quantification of the deep tissue oxygenation noninvasively. A unique capability of the sensor concept for simultaneous multiplexing of the sensor elements will enable development of a high resolution imaging system. The proposed R&D will make a novel sensor available at the clinic as well as at research facilities for reliable and cost effective applications.

The Phase I objective is to design and construct a breadboard sensor system based on the PRM-Correlation technique and Resolution Enhancement Technique using a near-ir diode laser. A proof of concept experiment will be performed in Phase I using a sub-nanosecond time resolution and a relatively large size simulated test-bed. Also, an extensive theoretical analysis and a simulation study will be performed to explore the imaging capability using multi-element sensor system. In Phase II prototype system, a temporal resolution of up to a few tens of picosecond will be implemented by modulating the diode at a few hundred MHz and applying the proprietary Resolution Enhancement Technique. The prototype sensor will be tested using a phantom with properties of a deep tissue and local absorbance simulating the cerebral applications. The preliminary medical testing of the prototype sensor will be arranged with one of the medical research centers (e.g. University of Maryland School of Medicine) and the commercialization of the sensor will be promoted. The sensor will be further developed to implement a multibeam transmitter and detector array system for rapid coverage of time resolved absorption measurements and imaging.

3. Breadboard Phase I System Description

In Phase I, with the limited time and resources, the development efforts were concentrated on the critical subsystems including a high bandwidth (~ 1 GHz) PRM generator and a high speed diode laser driver. High speed detectors are used throughout the experiment and a commercial high speed digital sampling oscilloscope was used as a data acquisition system. The overall system bandwidth was limited by the 1 GHz bandwidth of the digital oscilloscope in spite of the higher speed detector module.

The PRM generator module and the diode laser driver design are the state of the art in terms of speed and novel concept. Further improvement in Phase II will satisfy the entire system requirements for deep tissue oxygenation measurement. In this section, we elaborate the design features and performance characteristics of these submodules. They form the baseline for Phase II prototype system.

3.1 Pseudo-Random Code Generator

The pseudo-random modulation (PRM) codes used are M-sequence codes which have been commonly used. M-sequence PRM codes are the maximal codes which are the longest non-repeating codes that can be generated by a given shift register of a given length. The criterion for the maximal length is that the generating code polynomial, $1 + x^m + x^l$, be irreducible and prime over the Galios field where *m* is the feedback tap and *l* is the shift register length. If *m* and *l* are chosen correctly, the resultant bit sequence is pseudo-random. The M-sequence requires only minimal hardware and is the simplest to be implemented. It is also the most popular.

The basic properties of all maximal code sequences are as follows:

1. A maximal-length (n-bit) PN sequence has (n+1)/2 ones and (n-1)/2 zeros, where $n = 2^l - 1$.
2. The statistical distribution of ones and zeros is well defined and always the same.
3. Autocorrelation of a maximal linear code is such that for all values of phase shift the correlation value is -1, except for 0 ± 1 bit phase shift area, in which correlation varies from -1 value to 2^l-1 (the sequence length).

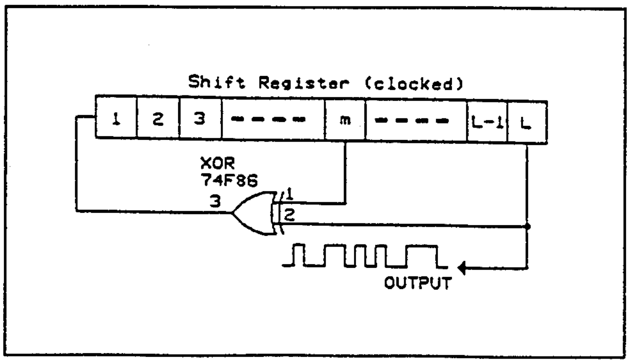

Figure 3.1 255 Pseudo-random bit sequence generator.

Figure 3.1 shows a fixed length $n = 2^l$-1 bit PN-Code modulator implemented with the feedback shift register. A shift register of length *l* bits is clocked at some fixed rate. An exclusive OR gate feeds back the serial input signal from the exclusive-OR combination of the

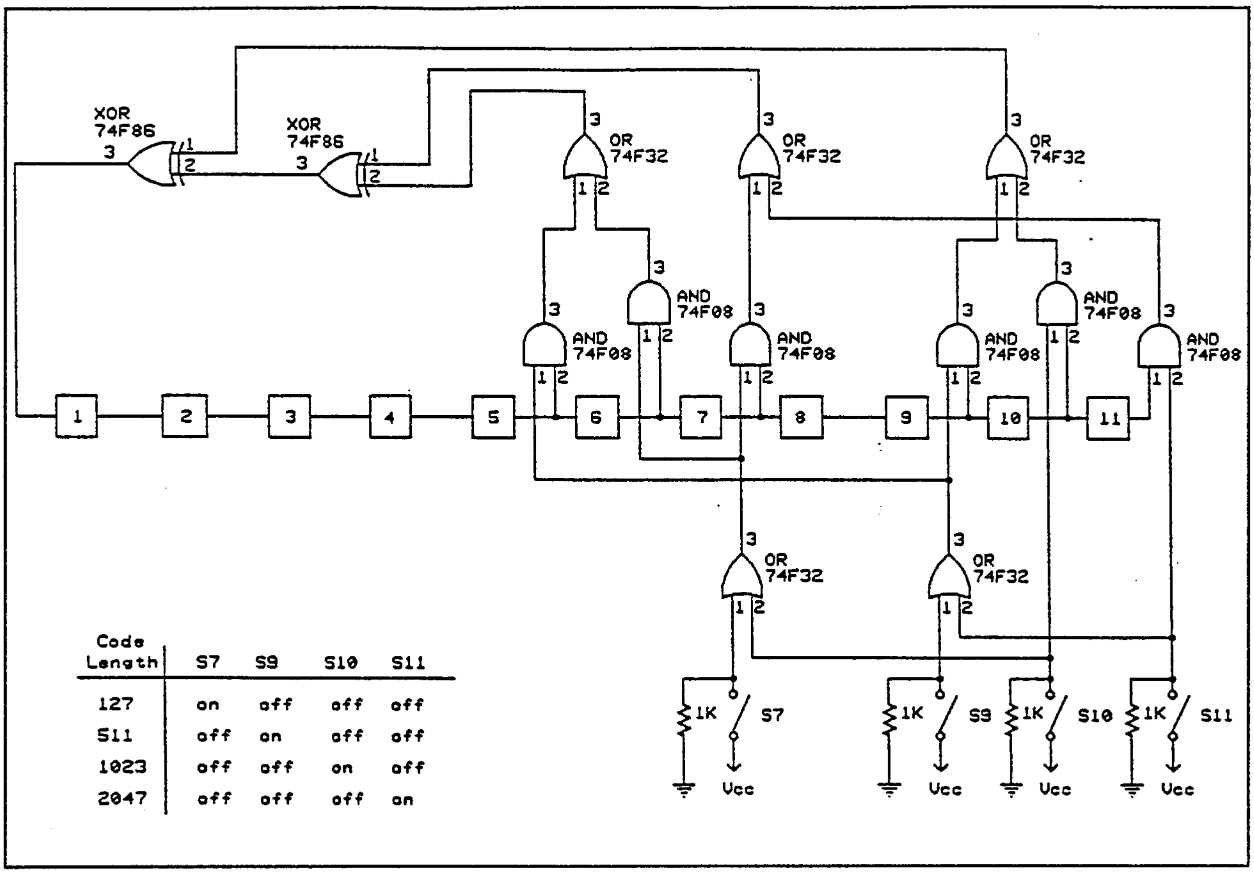

Code Length	S7	S9	S10	S11
127	on	off	off	off
511	off	on	off	off
1023	off	off	on	off
2047	off	off	off	on

Figure 3.2. Multi-pseudo-random bit sequence generator.

mth bit tap and the last stage lth bit of the shift register. The register has to be preset to all 1's before the register is clocked. The circuit goes through a set of states and repeats itself after 2^l - 1 clock pulses; i.e., it is cyclic with period of 2^l - 1. In binary shift register sequence generators, the maximum length sequence is 2^l - 1 bits. Figure 3.2 shows a logic diagram of multiple pseudo-random bit sequence generator. The design gives flexibility to select various bit sequence lengths. To maintain large bandwidth, only 2 feedback taps are implemented in the Phase I breadboard system.

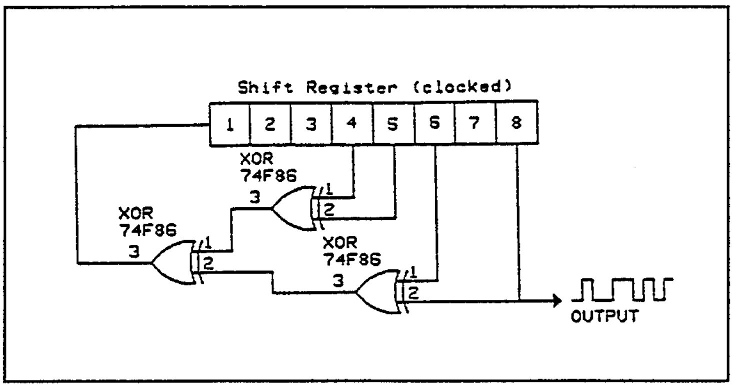

Figure 3.3. 255 pseudo-random bit sequence generator.

Maximal-length shift registers can be made from more than two exclusive-OR feedback taps. When more than two feedback taps are used, the delay inherent in the feedback loop accumulates along the path from the last stage l to the first stage 1. Figure 3.3 shows an example of PN code bit sequence generated by the polynomial $1 + x^4 + x^5 + x^6 + x^8$ which has 4 feedback points. The feedback path in Figure 3.3 requires more XOR gates than those in Figure 3.1 and each gate causes additional delay to the feedback path. Therefore, the limitation set by the feedback delay path defines the maximum useful speed of the sequence modulator. This two-feedback tap $1 + x^m + x^l$ polynomial configuration reduces the delays inherent in the feedback path. A value is given for m and for the cycle length $n = 2^l - 1$, in clock cycles. In some cases there is more than one possibility for m, and l-m can be used instead of m. Table 3.1 lists various maximal sequences available from register length l.

Table 3.1 Maximal Sequences Available For 2/4 Feedback Taps

Feedback Taps		PN Code Sequence Length (n)
l	*m*	
3	2	7
4	3	15
5	3	31
6	5	63
7	6	127
8	4,5,6	255
9	5	511
10	7	1023
11	9	2047

The PN code modulator prototype developed for this experiment uses high speed ECLinPS (ECL in Pico-Seconds) logic family. To obtain a high speed, only 2 feedback taps are implemented in the circuit design. The key elements are the two cascaded shift registers U2 & U3 (MC10E142's) which are clocked by the 200 MHz system clock. The selected pair of register outputs or feedback stages are directed to the inputs A_iB_i of the 2-bit 8:1 multiplexer U1 (MC10E163). The input pair A_iB_i propagates to the outputs Q_A & Q_B, which are programmed by setting the jumper JP1-3. The feedback pair QA & QB are then directed to the exclusive-OR (XOR) gate. The XOR output is feedbacked to the shift register input and the input is shifted into the register in the next clock cycle. The XOR output is then the desired PRM code.

The PRM code sequence is synchronized and restarted by an external TTL triggering pulse. The trigger pulse is detected by a pulse-catcher circuit which is only sensitive to the rising edge of the signal. The pulse-catcher generates a short ECL pulse with a minimum delay. The short pulse then resets the shift register and restarts the PRM code generation. The circuit also provides a clock dividing function; the 200 MHz system clock is divided into 100, 50, 25, and 12.5, etc.

The output of the PRM code generator is an ECL compatible signal with 50-ohm termination. It is fed to the laser diode driver to control the laser output. In operation, there were undesired signal noises and glitches generated. The signal-level-sensitive laser diode driver reflects all the noises in the laser signal. The dominating noise is generated by the racing of the propagating signals in the combined logic circuit. The racing problem can be eliminated in the output by directing the 1st stage of the clocked shift register to the output instead of the feedback signal. The high power ECL logic dissipates a large amount of heat. Nevertheless, a special heat sink for the small ECLinPS chip will be able to handle the thermal noises. Since the rise time of shorter than 1 ns is required in the circuit design, good terminations and signal transmission lines were used where possible. The interconnection distance, capacitive loading (fanout), resistive loading (line termination), and percentage of undershoot and overshoot (reduction in ac noise immunity) are the major concerns in the circuit design and fabrication. The signal bandwidth of the prototype is slightly greater than 1.0 GHz. The better signal quality can be easily accomplished for Phase II version of PN code modulator, based on the breadboard experience.

The next generation PRM generator is also designed with Motorola's ECL-in-Picoseconds (ECLinPS) advanced ECL logic family or Sony's SPECL standard ECL logic family ultra fast components. In order to generate at least 1.0 GHz modulation signal, only one PN modulation code sequence will be generated by a shift register. Some ECLinPS components are able to generate 3.0 GHz bandwidth signals. However, the printed circuit board (PCB) must be carefully designed, particularly in routing. High quality connectors and cables are important factors for achieving large signal bandwidth.

Three circuit diagrams are attached to this report in Appendix A, B, and C. They describe the clock circuit, the trigger circuit, and the PRM generator circuit respectively.

3.2 Diode Laser Driver

The laser diode driver is an ultra high speed GaAs hybrid circuit. The driver is to supply the DC bias and modulation current to the laser diode. The driver current is limited to 100 mA of DC bias and 50 mA of modulation. The modulation current is the peak-to-peak switching current. The maximum driving current is $100+50 = 150$ mA. The driver accepts single-ended ECL-format data. With the ECL switching signal input, the maximum current modulation rate is approximately 400 Mbps; the minimum rate is 10 Mbps. Figure 3.4 shows the design block diagram of the laser diode driver.

In this circuit, the GaAs FET Q1 is the data interface stage to the ECL data input. The input of the driver is connected to the PN Code generator to control the modulation of the laser. The switching, ON/OFF, stage of FET Q1 inverts the switching stage of FET Q2. When the FET Q2 is off, the input voltages of Modulation Control determine the V_{GS} of FET Q3. The maximum or saturation Drain current, I_{DS}, of the GaAs FET is controlled by V_{GS}. The Drain current of Q3 is the modulation current to the laser diode. The DC bias current is provided by a voltage controlled current source. The amount of DC bias current is proportional to the input voltage. The GaAs power FET is capable of operating up to 20 GHz frequency range. Therefore, the modulation frequency range is not limited by the laser driver electronics.

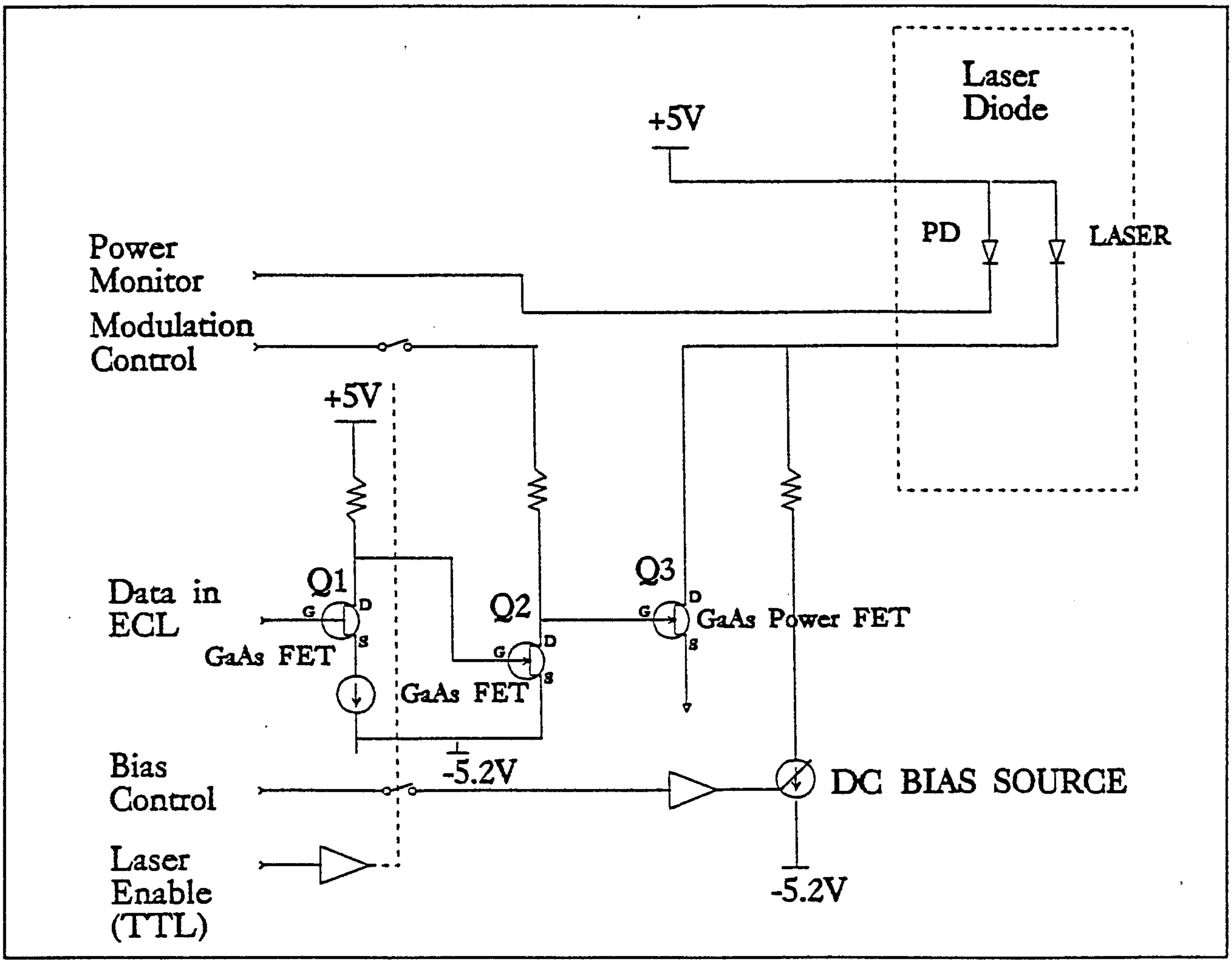

Figure 3.4. Block diagram of laser diode driver.

The laser diode is the limiting element for the modulation speed. It commonly responds with 500 picosecond rise time due to internal capacitance.

The Laser Enable is a TTL digital input which controls the laser power ON/OFF. The laser driver also contains circuits for soft-start and sequencing to protect the laser from the surge current. The driver contains trimmer pots, marked ‘Bias Adj’ and ‘Mod Adj’. These trimmers allow the user to set the bias and modulation currents without using external supplies connected to the bias and modulation set pins. In this mode of operation, the only required external connections are +5V, -5.2V, Laser Enable, and ECL data input.

3.3 Detector and Data Acquisition System

Detectors

Two different high speed detectors were used for the system to measure the reflection or transmission signal. A high speed silicon Avalanche Photo Diode (APD) and a PMT with multi-alkali cathode were used in the experiment. The APD (Opto-Electronics, Inc., Model AD230, 3 GHz bandwidth) used here has a high quantum efficiency but with only a nominal gain of less than 100. A simple calculation shows that the photon diffusion signal of a 50 mW transmitter at a 10 cm distance is about 0.5 μW. This signal is marginal for detection by the detector with noise equivalent power of 0.1 μW. As a result, the measurements for large separation distances over 10 cm were not very reliable, due to the signal induced noise. This limitation of the signal strength can be overcome using larger area collection optics with an expense of spatial resolution. Nevertheless the calculation indicates that the sensitivity will be high enough for short separation distance measurement for the phantom. Thus a limited data set was obtained using the APD for short separation distances up to 6 cm. The high bandwidth available with the APD, however, was not fully explored in the experiment due to the limited bandwidth of the digitizer used. Consequently the data obtained for the short separation distance measurement was not best suited for the quantitative analysis for optical parameter retrieval.

In order to clearly demonstrate the quantitative measurement capability of the technique with the limited system bandwidth, we rely on the large separation distance measurement. For this purpose we have employed a high speed PMT (Hamamatsu, H5783-01) which has a limiting bandwidth (0.65 nsec rise time). Nevertheless the high sensitivity of the PMT provides us a measurement capability over a large separation distance which then allows us to make quantitative measurement of the optical parameters of the phantom for varying absorber concentration. The temporal response of the breadboard system was then obtained by taking one set of data with an empty cell in the beam path. This system response function represents the total system bandwidth. It is important to note that the current system bandwidth is slightly less than 1 GHz, which should be adequate for all planned experiments at the present.

Data Acquisition System

A commercial sampling oscilloscope was used for data acquisition instead of the custom developed data system. A high speed (1 GHz bandwidth) LeCroy 9324 oscilloscope is directly used to digitize the detector output signal without any amplifier. The sampling resolution of this system is as high as 10 GHz, thus the temporal precision of the data is equal to 100 psec. Signal average is carried out on the oscilloscope directly before a data set is acquired onto a computer. The oscilloscope is triggered by the same trigger pulse for the PRM generator, thus the data acquisition is always synchronized to the laser transmitter modulation. For the APD detector, the breadboard system bandwidth is limited by the oscilloscope bandwidth, and the PMT response time was found slightly slower than the digitizer speed.

A high speed digitizer system with over 1 GHz bandwidth is designed for the prototype Phase II system based on the custom ordered ASIC chip. A commercial digitizer of a comparable speed is also projected to be available within a year in time for the Phase II development. A detailed design, to be described in Section 5.2, will be fully implemented for wide bandwidth (over 1 GHz) and high precision (better than 40 psec) data system using the delay generator circuit and the high speed ADC chip in Phase II.

3.4. Optical Implementation of the PRM Technique

An example of PRM code with length 127 bin is shown in Fig. 3.5. The upper plot is the code in its ideal digital format and the lower plot is the code generated by our PRM code generator ECL circuit at 200 MHz modulation speed. The ECL output is connected to the laser diode driver to modulate the diode laser bias current. The laser output measured by a detector is plotted in Fig. 3.6. Most of the experimental results shown in this report are from lasers modulated at 200 MHz speed, as shown in the upper plot of Fig. 3.6. However, toward the end of Phase I period we upgraded the PRM code generator to 400 MHz. The diode lasers were tested at this modulation speed and a typical response is shown in the lower plot of Fig. 3.6. By increasing the modulation speed from 200 MHz to 400 MHz, the width of the instrument function is narrowed by a factor of two, as shown is Fig. 3.7. Notice that the instrument function is defined as the correlation of the laser response and the PRM reference code. We plan to experiment with 400 MHz modulation speed in Phase II to achieve higher measurement sensitivity than what we achieved so far at 200 MHz. With narrower instrument function, the slope of the correlation function will be more sensitive to small changes in absorption where large scattering dominates the correlation function. In addition, the first moment may also be determined more accurately so that the measurement is more sensitive to both absorption coefficient and scattering coefficient changes.

3.5. Breadboard PRM/RET System Characteristics

Breadboard system consists of a 200 MHz PRM generator, 1 GHz bandwidth diode laser driver, 0.8 or 1.5 GHz detector, and 5 GHz sampling oscilloscope. The sampling scope also function as a precision delay generator. As will be further discussed in the next section, a 40 psec measurement precision has been accomplished through the RET implementation.

It is important to note that the temporal precision of the breadboard system is significantly higher than the system response time; the temporal precision of the system is defined by the ability of measuring the temporal position. In our system, the precision is governed by the precision of the delay time which is better than 50 psec. Further improvement beyond the delay precision is also possible for other statistical analysis of the measured pulse profile.

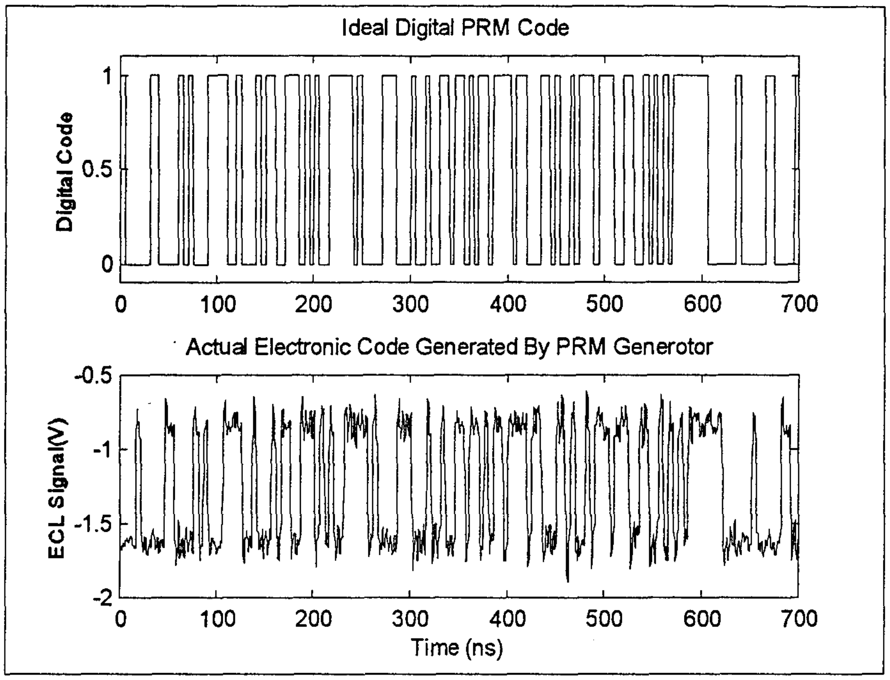

Figure 3.5. M-sequence PRM code with 127-bin length. (A) Ideal digital code; (b) Actual electronic code from the PRM generator ECL circuit.

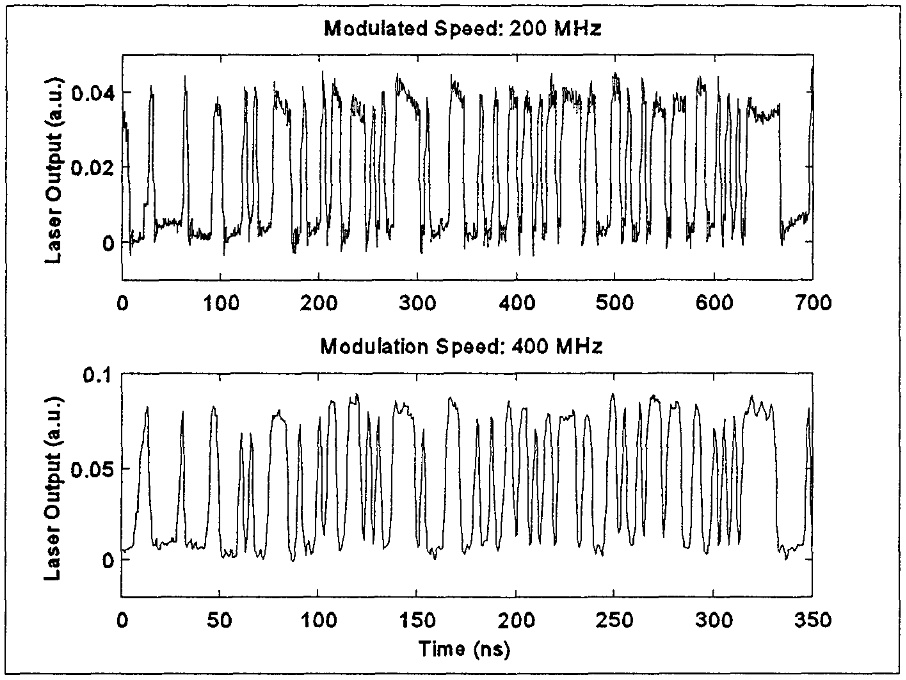

Figure 3.6. Diode laser response to PRM modulation at (a) 200 MHz and (b) 400 MHz speed respectively.

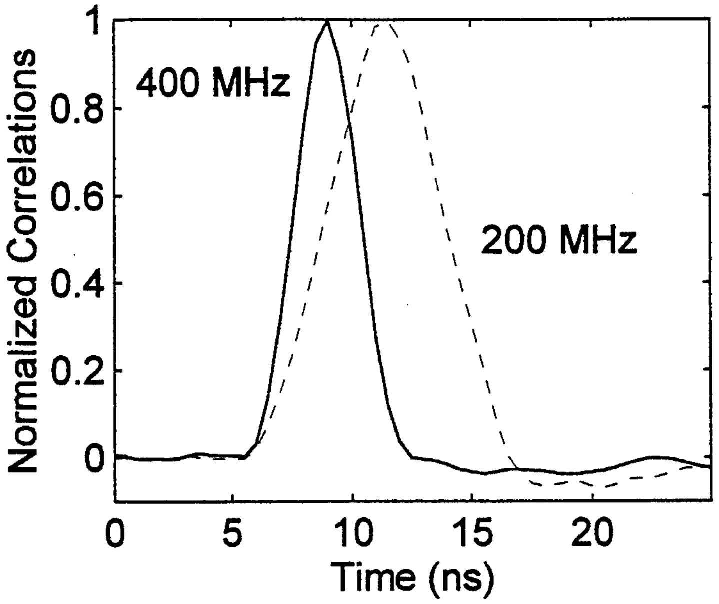

Figure 3.7. Comparison of correlation function with two different modulation speeds: 200 MHz and 400 MHz.

4. Feasibility Experiment

Feasibility experiment performed in Phase I encompasses various aspects of the PRM/RET technique. The verification of RET is first discussed, and experiments on tissue phantoms using the breadboard system follows. In that, the quantitative experiment defines the accuracy of the optical parameter measurement. Then experiment for simple robust application of the system for optical parameter measurement of the tissue phantom is carried out. Theoretical background for data analysis are also included in this section.

4.1 Verification of PRM/RET Technique by Accurate Time Delay Measurement

A direct verification of the Resolution Enhancement Technique is presented here using 200 MHz PRM modulation and 2 GHz digitizer sampling rate. Using this PRM/RET system, we demonstrate 40 psec time resolution for accurate measurement of photoelectron transit time in a PMT. The experimental setup measures the temporal location of the photoelectron transit time spread for various PMT bias voltages. The standard deviation of thus measured transit time from the theoretical function then provides the limiting uncertainty.

When photomultiplier tubes are used for the time-resolved photonic measurement on the nanosecond time scale, it is important to recognize that the photoelectron transit time is dependent on the applied PMT voltage. This can be easily understood by examining the physical principles of photo-multiplier operation. The photoelectrons generated at the cathode are accelerated to the first dynode. The number of electrons are multiplied at the dynode by producing secondary electrons. This multiplication process continues on each successive dynode. The time it takes for the photoelectrons to multiply and finally reach the anode depends on the bias voltage between each dynode since the terminal velocity of electrons is directly related to the kinetic energy gain through the consumption of the electric potential energy sustained by dynodes. In this process, the transit time of the photo-electron across the dynodes can be expressed as

$$t_d = \frac{C_{PMT}}{\sqrt{V}}$$

where t_d is the transit time, V is the applied PMT voltage, and C_{PMT} is a constant dependent on the PMT geometry.

Figure 4.1 shows the relation between t_d and $1/\sqrt{V}$. In our data analysis, we define the average measured transit time as the first order moment of the measured correlation function which is equivalent to the photoelectron temporal spread function, P. That is

$$t_d = \frac{\int t P(\rho,d,t)\,dt}{\int P(\rho,d,t)\,dt}$$

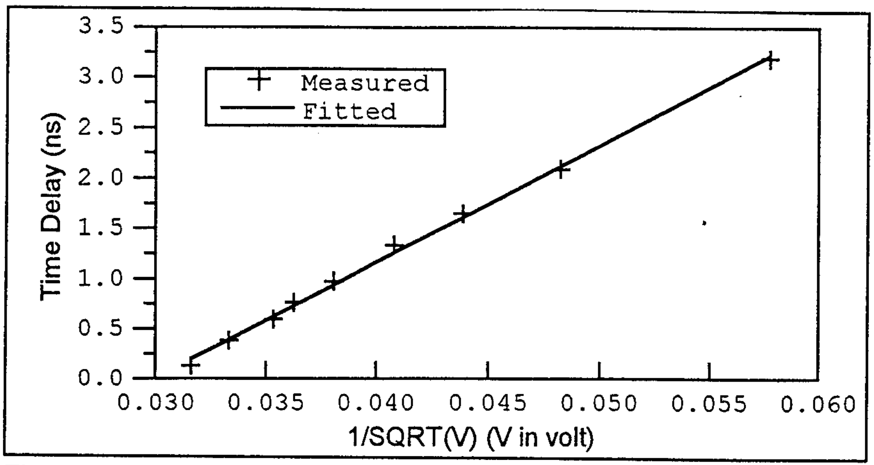

Figure 4.1.. Relation between PMT voltage and time delay. The standard deviation of the measurement to the theory is 40 psec.

The symbol '+' in Fig.4.1 represents the measured data points, and the solid line represents the linear-least-square fit to the data. A standard deviation of 40 psec is calculated from this data set. It actually represents the effective resolution of the PRM/RET measurement. This result demonstrates an over 100 fold improvement of the temporal resolution of the PRM/RET system over the quantization limit of the PRM technique, clearly demonstrating the extension of the novel technique into the subnanosecond range. It is important to recognize that this resolution is directly applicable for accurate temporal measurement of the deep tissue response function together with the unique synchronization capability of the PRM/RET.

4.2 Pathlength Dependent Photon Migration in Phantom

In the reflection measurement mode, the photon migration paths are strongly dependent upon the transmitter/detector separation distance for a given medium optical properties. In general, for short separation distances, most of the photon migration paths are confined to the region near the surface. As the separation distance increases, more photons migrate deeper into the medium. Thus it is important to select the optimum separation distance to reach certain penetration depth of the average migrated photons. Since the photon migration paths are substantially different for different separation distance, the Environmental Response Function (ERF) depends on the separation distance. The ERF represents the measured temporal waveform of the phantom which is the convolution of phantom impulse response function (IRF) and the system response function. This is also the same as the convolution function of the PRM time series data with the reference code. The breadboard system is used to measure the ERF of the skim milk phantom at various separation distances. The transmitter was pointed to a spot on the side of the cylinder and the detector position was varied along the circumference of the cylinder for various distances between 3 cm and 7 cm as shown schematically in Fig.4.2 together with a photograph of the actual setup. An SiAPD (4 mm dia) was initially used without any additional collective lens for a good spatial resolution. However, for larger separation distances the signal becomes too small and the APD excess noise becomes apparent above the signal level, thus the data was unreliable.

We confine the measurement using the PMT within 6 cm separation distance. A typical, measured ERF is plotted in Fig. 4.3. Together with the measured ERF, also plotted are the theoretical ERF (solid line) based on the diffusion theory. The overall quality of the data is very good and the measurements reproduce the theoretically predicted ERF very closely as can be noticed in the figure.

A new convolution technique using the measured PRM function from the reference phantom (without scattering and absorption medium) in place of the theoretical PRM function was developed and used for further data analysis. In this technique, the PRM Autocorrelation Function (PRMAF) represents the actual total system response which precisely accounts for the total system bandwidth. Furthermore, this function accounts for any residual system nonlinearity accurately. Thus when this PRMAF is used for the convolution, the theoretical ERF function should represent the measured ERF precisely. Data discussed in the next section are processed using this technique to obtain high accuracy tissue parameter.

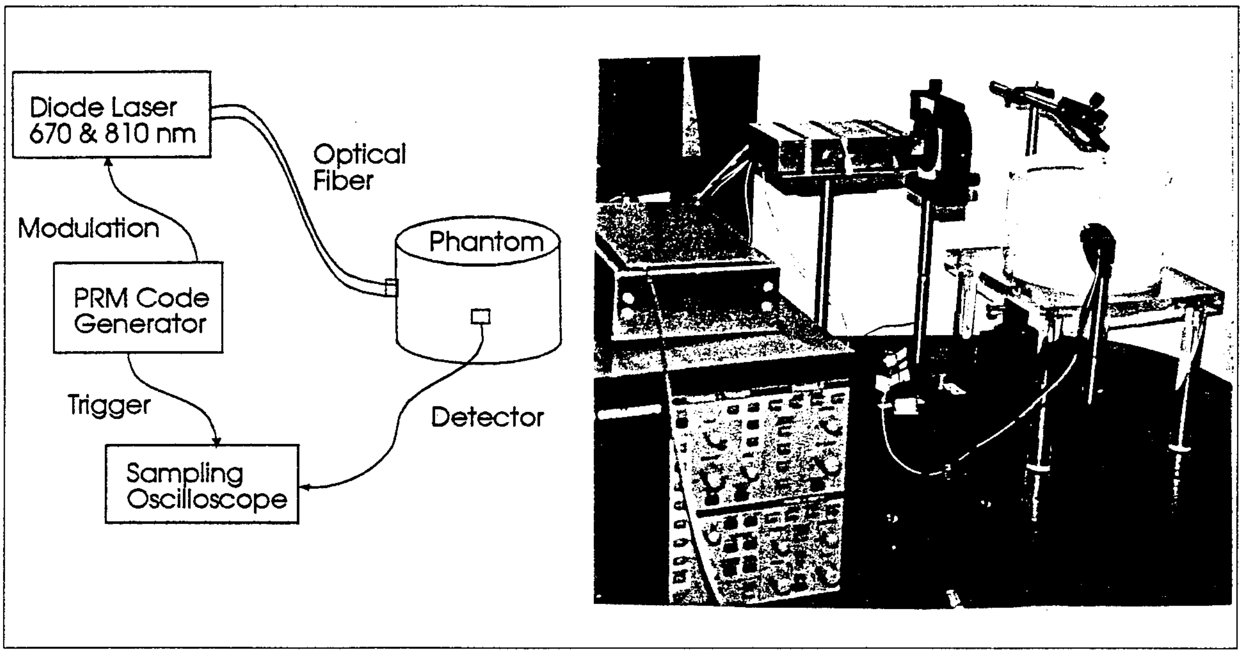

Figure 4.2. Schematics of the experimental setup for phantom measurement with a photograph of the actual setup.

These data from the breadboard system clearly demonstrate the powerful capability of the PRM/RET sensor for measuring the pathlength dependent photon migration within a phantom which is relevant to the deep tissue environment. This is the first of a kind data set obtained using the PRM/RET technique developed in this program, thus represents a preliminary result. Nevertheless, the quality of the data appears to very well satisfy the quantitative measurement requirement. For the large penetration depth into the deep tissue and quantitative measurement of the blood oxygenation, we study the cases with even larger separation distances. In the following section we present the quantitative measurement results with a large separation distance.

4.3. Quantitative Optical Parameter Retrieval by PRM/RET Measurement

The expected IRF is calculated from the solution to the diffusion equation in terms of the photon density, P, ($\mathrm{sec}^{-1}\ \mathrm{cm}^{-2}$) per incident photon:

$$\phi(t) = c(4\pi Dct)^{-3/2}\exp(-\frac{\rho^2}{4Dct} - \mu_a ct)$$

where $D=1/3(\mu_a+\mu'_s)$ is the diffusion constant, μ_a is the absorption scattering coefficient, μ'_s is the effective scattering coefficient, c is the light velocity in the medium, and ρ is the separation between source and detector.

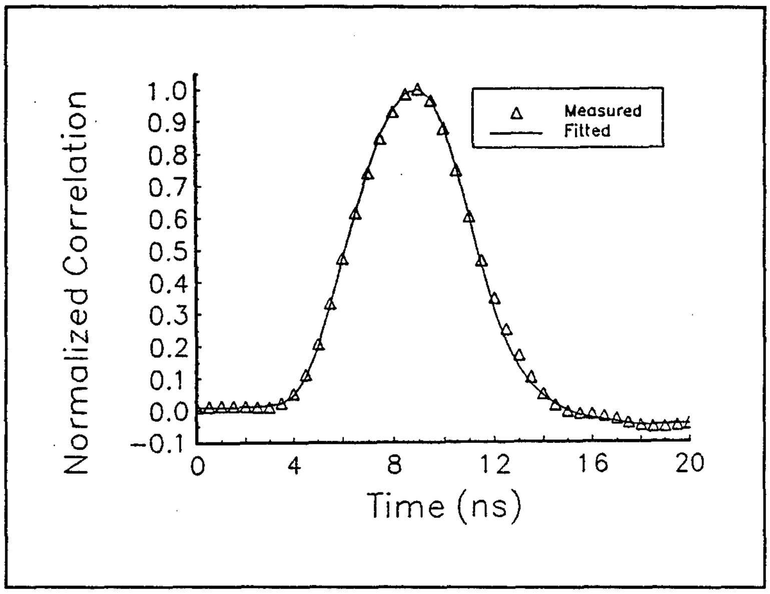

Figure 4.3 Comparison of a measured ERF with a theoretically calculated ERF.

In order to obtain the analytical expression of measurable quantity photon flux coming out of the tissue, Patterson et al [1989] derived the time resolved reflectance and transmittance of light due to tissue scattering and absorption based on the assumption that the tissue has a finite thickness d and is boundless in the horizontal directions. Based on this semi-infinite homogeneous medium model, the photon flux detected under the tissue slab at a separation distance d from the incident light and a distance ρ from the incident beam is proportional to the transmittance

$$T(\rho,d,t) = (4\pi Dc)^{-3/2}t^{-5/2}[\exp(-\frac{\rho^2}{4Dct} - \mu_a ct)]\, f_t(d)$$

where

$$f_t(d) = (d-z_0)\exp[-\frac{(d-z_0)^2}{4Dct}] - (d+z_0)\exp[-\frac{(d+z_0)^2}{4Dct}]$$

$$+(3d-z_0)\exp[-\frac{(3d-z_0)^2}{4Dct}]-(3d+z_0)\exp[-\frac{(3d+z_0)^2}{4Dct}]$$

and

$$z_0=1/[(1-g)\mu_s]$$

The reflected photon flux detected on the upper surface of the slab is proportional to the reflectance

$$R(\rho,d,t)=(4\pi Dc)^{-3/2}t^{-5/2}[\exp(-\frac{\rho^2}{4Dct}-\mu_a ct)]\,f_r(d)$$

where

$$f_r(d)=z_0\exp(-\frac{z_0{}^2}{4Dct})-(2d-z_0)\exp[-\frac{(2d-z_0)^2}{4Dct}]+(2d+z_0)\exp[-\frac{(2d+z_0)^2}{4Dct}]$$

The System Response Function and Correlation Calculation

The laser output will follow the bias current modulation waveform provided that the bandwidth of the diode is large enough. In the transillumination measurement experiment, we use an M-sequence code with a length of 127 bin and modulation frequency of 200 MHz as depicted in Fig. 3.5(b) on page 15. The optical signal is detected by a fast detector (either Hamamatsu PMT model 5783-01 or Opto-electronics, Model AD230) and the output of the detector is directly digitized by a sampling oscilloscope (LeCroy model 9024). The sampling rate of the scope is normally set at 2 GHz and a total of 2,000 number of points are taken for each sweep. The sampling scope also performs the data averaging to enhance the signal to noise level. Usually 300 to 1,000 sweeps are averaged to obtain one data set.

A diode laser, Hitachi Model HL7851G, is used in this experiment. The emission wavelength of the diode laser is 780 nm with its maximum output power of 50 mW. The laser is biased with a DC current of 30 mA, which is just below the lasing threshold. Then the PRM current is summed to the DC bias and applied to the laser through the laser diode driver. The bandwidth of the diode laser is expected to be better than 1 GHz and thus the laser output intensity should follow the current modulation with a high fidelity. However, due to the noise introduced by the random code generator, the laser output was not a perfect replica of the theoretical PRM code waveform. Furthermore, the PMT detector with a rise time of 0.65 ns and a decay time of 1.5 ns further distorts the optical waveform when it is modulated with a higher than 1 GHz bandwidth (not necessarily the modulation frequency). A typical laser output waveform measured by the breadboard setup (detector and digitizer system) in the absence of the scattering medium is shown in Fig. 3.6(a) on page 15. Since beam does not pass through any scattering medium, this waveform is actually the net response function of the detection system consisting of the modulated laser, the fast detector, and the sampling oscilloscope. We call this waveform the system response function, *H(t)*, and it is used in our data analysis to convolve with the IRF of the phantom to accurately predict the ERF measured in the experiment for each optical parameter.

For the phantom filled with the scattering medium with a certain scattering and absorption coefficient, the transmittance (time dependent) of light will be described by the diffusion equation. If we use PMT to collect the transmitted light, the detected signal *S(t)* should be the convolution of the system response function, *H(t)*, and the theoretical phantom transmittance function, IRF. That is,

$$S(\rho,d,t) = \int H(t-\tau)\, T(\rho,d,t)\, d\tau$$

The detected signal *S(t)* is then correlated with the PRM code to obtain the correlation function which is the measured ERF. For the phantom filled with scattering medium, the correlation function, ERF, will have a rising and falling edge resembling that of the phantom IRF. Deconvolution of the system response function from the ERF to obtain the IRF becomes unstable for the noisy data. Therefore, to retrieve the information of the scattering and absorption coefficients, we analyze the ERF directly.

4.4 Data Analysis Algorithm

Unlike in the picosecond laser based TRS sensors, the ERF is significantly broader than the phantom IRF due to the large width of the PRM autocorrelation function. The most elegant way of analyzing this type of data is to deconvolve the system response function (the autocorrelation function of the signal without sample) from the ERF to obtain pure IRF of the phantom being measured. Although straight forward in concept and also works well with the ideal data set with no noise, deconvolution of the system response function of step function profile is not trivial in the presence of realistic noise level. Due to this difficulty, we have explored alternative methods which can be applied for the optical parameter retrieval without the deconvolution.

Nonlinear Curvefit

Without resorting to the deconvolution, there are two general approaches for retrieving μ_a and μ'_s from the convolved signal: nonlinear least square fit and characterization of statistical properties of the signal shape in the time domain. The most straight forward method is to apply a nonlinear χ^2 curve fitting routine using the solution of the photon diffusion equation. Here χ^2 is defined as

$$\chi^2 = \Sigma[(\rho_m - \rho_f)^2/\rho]$$

where ρ_m and ρ_f are the measured and the fitted correlation functions respectively, and ρ is the mean of the measured and fitted correlation function. The optical parameters of the phantom is derived by minimizing the χ^2 value for a wide range of variation. A specific simplified technique of accounting the system response function for the theoretical ERF functions for each phantom parameters are developed for the data analysis. In this technique the measured PRM codes using the actual sensor system is used to convolve the IRF of the phantom to obtain predicted PRM signal which is in turn used to calculate the predicted ERF. This predicted PRM signal, therefore, represents the measured PRM signal accurately accounting entire system bandwidth and other biases. This technique works remarkably well for the predicted ERF calculation mainly due to the unique noise filtering property of the PRM correlation calculation process. In this process, the system response function, which is measured in the absence of the phantom in the experimental setup, is convolved with the phantom response function to reproduce the measured signal. Normally, broad minimum exists for the tissue data and the optical parameters are uniquely defined.

One of the significant benefit of this approach is the precise synchronization of the predicted phase with the measured ERF as shown in previous results. The nonlinear fitting result in Fig. 4.3 does not require any phase adjustment between the two ERF's, measured and predicted, and yet shows accurate synchronization. This property provides a unique advantage of the PRM/RET technique compared to other TRS or PMS systems, by allowing precise positioning of the maximum likelihood of the ERF peak position.

Statistical Algorithm Based on the Moment Analysis of the ERF

A nonlinear least square fit, although very accurate, is not an efficient approach in terms of the efficiency of the numerical computation. For the real time application, we explore a simple algorithm for the optical parameter retrieval based on the statistical character of the ERF.

The approach here is to numerically calculate some properties P_i, of the temporal shape of a ideal ERF function, over a grid of values of μ_a and μ'_s, and repeating this for a number of properties, N. Then one has N two-dimensional tables of $P_i(\mu_a, \mu'_s)$ which form a Cartesian grid in μ_a and μ'_s. One may rearrange the tables to obtain $\mu_a(P_1, P_2, \ldots, P_N)$, and $\mu'_s(P_1, P_2, \ldots, P_N)$. These two tables do not form Cartesian grids in the properties' N dimensional space. So finding μ_a and μ'_s for an arbitrary measured set of properties requires an interpolation in this non-Cartesian space.

In order to use this interpolation method, one must assure that the sensitivity is sufficiently large and that the signal shape properties are insensitive to noise. Properties tested are the first through fourth moments, and characteristics of the waveform integral. The first moment is

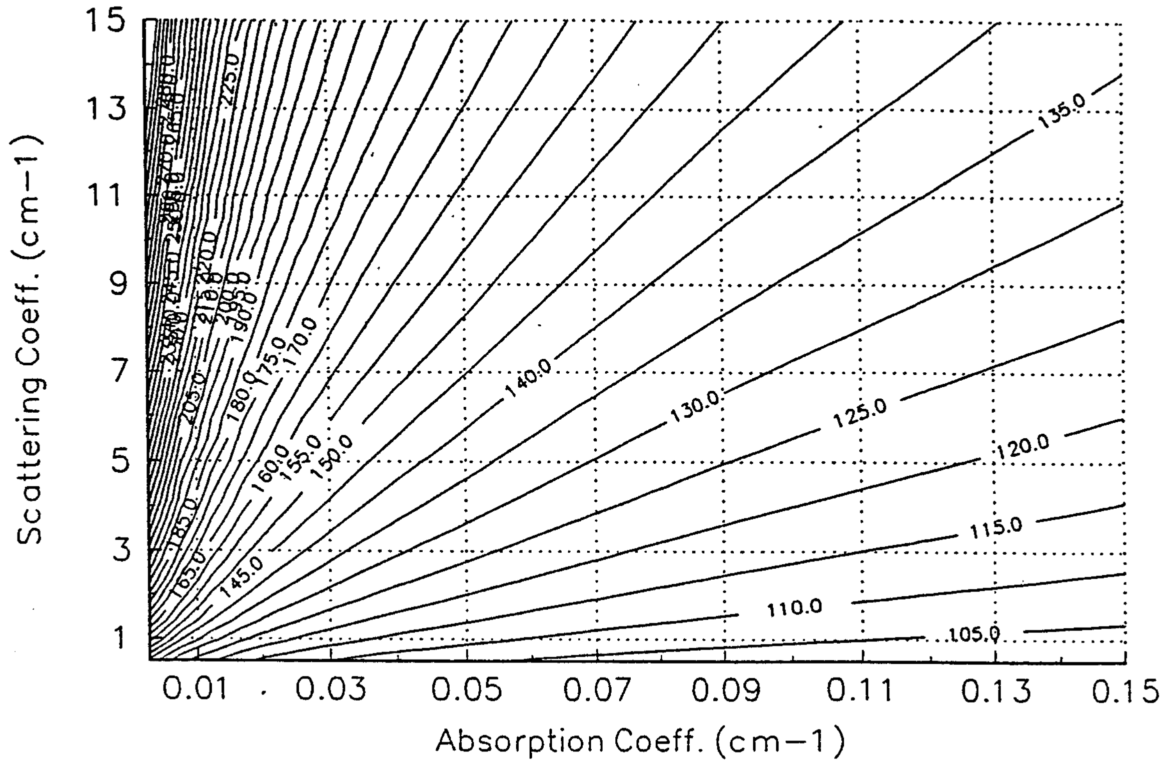

Figure 4.4 Contour of first moment of the ERF over a wide range of optical parameters from a simulation study.

relatively insensitive to noise. Figure 4.4 shows the first moment obtained from a simulation calculation as a function of μ_a and μ'_s and without noise. It shows an excellent and almost linear functionality over the entire domain of the optical parameters of interest. The noise dependency of the map is relatively small. The second, third and fourth moments can be calculated around the maximum likelihood peak position and may represent changes on ERF profile.

Fractional Threshold Width

Another alternative algorithm may be developed based on the ERF width measurement. Assuming the PRMAF and IRF are statistically independent, the net ERF width may be predicted by a square root of the addition of the each variance [Lee, 1984]. Therefore the width of the ERF will represent the IRF properties in the presence of the perturbation by the PRMAF width which is fixed for a given sensor. We explored the potential of this algorithm briefly in this program. Further study is planned in Phase II.

4.5 PRM/RET Measurement of Phantom Optical Parameters

A two step process is taken to demonstrate the remarkably quantitative measurement capability of the PRM/RET breadboard system. The first step is to measure the optical parameters of a simple solution with known linear behavior as the concentration of the solution is systematically changed. The data from the PRM/RET measurement is then verified quantitatively from this measurement based on the *a priori* knowledge. The measurement accuracy is then defined from this result based on the standard deviation of the measurement. The second step is to apply the PRM/RET technique, with the simple first moment algorithm, to the varying optical parameter of a phantom and define the sensitivity of the measurement.

The performance of the sensor is characterized by a moderate PRM modulation frequency of 200 MHz and an effective sampling rate of 2 GHz. The effective system bandwidth is approximately 1 GHz when a high speed APD is used and slightly less than that when a high speed PMT is used. Using this sensor an experimental setup was prepared to demonstrate an over 100 fold improvement of the time resolution of the conventional PRM technique providing 50 psec effective time resolution.

4.5.1. Retrieval of Optical Parameters Using Non-linear Curvefit

Based on this time resolution, we have devised proof of principle experiments using various model phantoms resembling the soft tissue characteristics. One of the phantoms consists of a milk solution, and the scattering coefficient and absorption coefficient of the model are manipulated by adjusting the milk and an additive ink concentration. Both reflection and transmission measurements were carried out using the PRM/RET sensor. The experimental response function (ERF) of the net phantom response, with the instrument function convolved, are obtained for various parameter settings of the phantom. The measured ERF is then analyzed by a nonlinear χ^2 fitting of a theoretically predicted waveform. A new technique of convolving the exact instrument function was developed. Based on this technique, the χ^2 fitting provides a remarkable capability of reproducing the measurement as shown in Fig.4.3 on page 20.

Measurements of the scattering and absorption coefficient of the phantom at various milk concentration were made using PRM/RET sensor and the nonlinear curvefitting algorithm. The triangular symbol in Fig.4.5(a) and Fig.4.5(b) represents the measured scattering and the absorption coefficients obtained through this nonlinear fitting versus milk concentration, respectively. The linear relationship between the milk concentration and measured absorption and scattering coefficient is clearly borne out in this data set indicating the validity of the data from the PRM/RET measurement. It is important to recognize that the milk is a one component solution, thus linear variation is expected as the concentration varies, in principle. The data is also extrapolated to the zero milk concentration by extending the linear-least-squares fit of the data, as shown by the dashed lines. Notice that the zero milk concentration should actually provide the scattering and absorption coefficient of water. Comparing these values from the extrapolation with the published data [Wolfe and Zissis, 1978], we find an

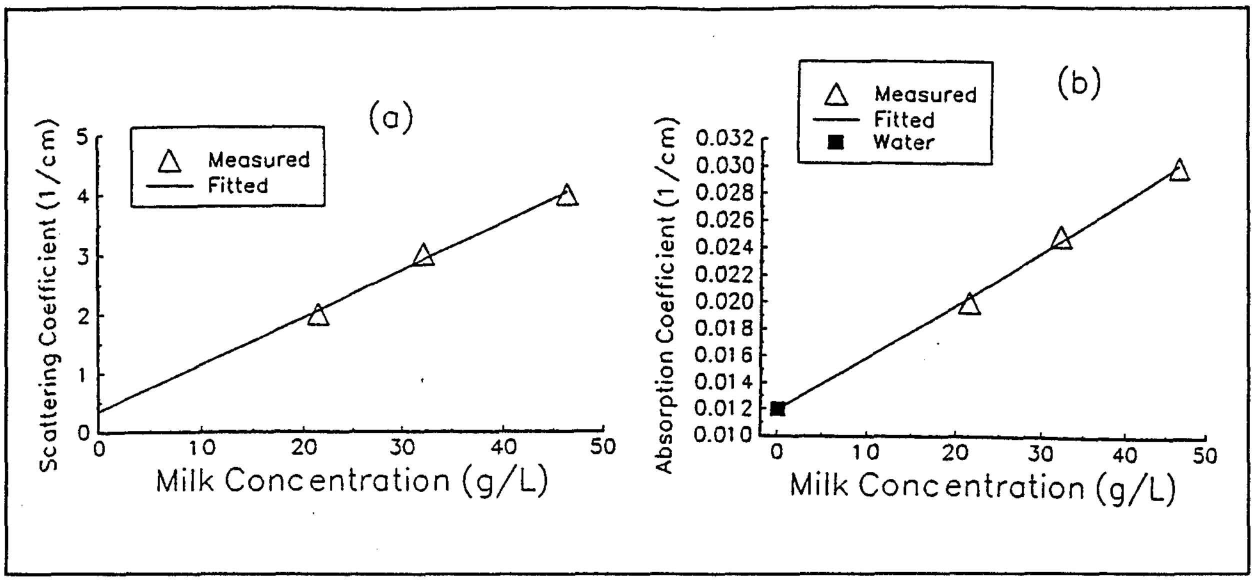

Figure 4.5 Measured and linearly fitted (a) scattering coefficient, (b) absorption coefficient

excellent agreement indicating the accuracy of the PRM/RET technique independently.

The measurement accuracies of 0.001 cm^{-1} for absorption coefficient and 0.07 cm^{-1} in scattering coefficient were obtained from the standard deviation in this data set shown in Fig.4.5. This accuracy is sufficient to differentiate a few percent variation of oxygenation of deep tissue blood. Considering the capability of deep tissue penetration of the signal in reflection measurement by optimizing the separation distance of the light source and detector, the above measurement accuracy offers a significant benefit in the clinical applications.

To retrieve the scattering and absorption coefficients from this data set, we apply the nonlinear χ^2 fitting with theoretical curves predicted from the diffusion equation. Table 4.1 lists the reduced chi-squared value for each data set. The overall χ^2 value is remarkably small insuring over 99% confidence level of the fitting for all data sets.

Table 4.1 Reduced χ^2 in obtaining μ_s from data shown in Fig. 4.5.

Data Set	1	2	3	4	5	6	7
χ^2	0.002	0.003	0.004	0.01	0.02	0.02	0.05

In conclusion, the measurements and data analysis clearly demonstrate a remarkable capability of the PRM/RET sensor for quantitative measurement of brain tissue absorption coefficient with an accuracy of 0.001 cm^{-1}. This measurement accuracy corresponds to accuracy of blood oxygenation of 1~2% measurement in a noninvasive mode. Based on this accuracy and robust operational characteristics of the sensor configuration, this technique clearly offers a unique opportunity in real time clinical applications for emergency patient and other deep tissue diagnostics requirements.

4.5.2. Retrieval of Optical Parameters Using First Moment

First Moment Measurement for Varying Absorption Coefficient of Intralipid Phantom

One of the important features of the PRM measurement is the high sensitivity of the peak value to the optical parameters. As proposed in the Phase I proposal, the maximum likelihood position of the pulse peak as calculated by the first moment of the ERF waveform was critically analyzed using the data set from an intralipid phantom. This parameter (first moment) can be very accurately calculated from the PRM data due to the accurate and consistent synchronization between the laser modulation waveform and the data acquisition timing. As discussed in Section 4.1, a 40 psec accuracy in the first moment measurement was demonstrated in an independent experiment. Therefore the hypothesis of high sensitivity of the first moment to the tissue optical parameters are tested in the feasibility experiment.

In this experiment, the phantom was made of 0.5% intralipid solution filled up to 6.5 cm height of a cylindrical container with a diameter 15.1 cm. The reduced scattering coefficients are estimated to be 10 cm^{-1} and 5 cm^{-1} at 670 nm and 809 nm respectively, while the absorption coefficients are estimated to be 0.06 cm^{-1} and 0.002 cm^{-1} respectively [Duncan, et al., 1993]. To increase the phantom's absorption coefficient, we added five-times diluted Parker Ink to the intralipid solution and stirred the phantom until it was visibly uniform in color. The maximum amount of ink added to the intralipid solution was 12 cm^3. This is only 1% of the phantom's volume and it's effect to the phantom height is therefore negligible. The absorption coefficients of the diluted ink was determined by an independent transmittance measurement using 2 mm and 5 mm pathlength cuvette. They are 30 cm^{-1} at 670 nm and 0.36 cm^{-1} at 809 nm.

Two lasers emitting at wavelengths 670 nm and 809 nm respectively were used in a differential transmittance experiment with a setup as shown in Fig. 4.2. Each laser beam was first collimated by a lens and then sent to a beam combiner. The combined beam was then coupled to a 3M Power-Core multimode fiber with a core diameter of 50 microns. Both ends of the fiber is connected with a coupling lens package. The average optical power actually delivered to the top surface of the phantom was about 28 mW at 670 nm and 63 mW at 809 nm. A PMT detector was placed at the bottom of the phantom to measure the transmittance.

I) Transmission measurements

The result of the transmission experiment, with the transmitter fiber at the top of and the detector at the bottom of the cylinder, is plotted Fig.4.6. The first moment *vs.* the absorption coefficient of the phantom is plotted for two different scattering coefficients. Zero value in first moment represents the measurement with no phantom in the container. Extremely high sensitivity of the first moment to the absorption coefficient change is clearly demonstrated in this plot. For the normal tissue condition, the variation of absorption coefficient is expected to be anywhere between 0.05 and 0.18 cm^{-1} which is at the mid range of our experimental data. In this range, the accuracy of measurement is calculated to be 0.0045 cm^{-1} based on the slope of the data and 50 psec resolution of the present PRM sensor. This corresponds to a few percent accuracy in oxygenation of the hemoglobin assuming the tissue absorption is in the range of 0.1 cm^{-1}. We note that the first moment measured here is a robust output parameter of the PRM sensor in terms of its insensitivity to the random noise, interference from other instrument, etc. This robust characteristics and high sensitivity is what makes the PRM technique very well suited for the battlefield applications.

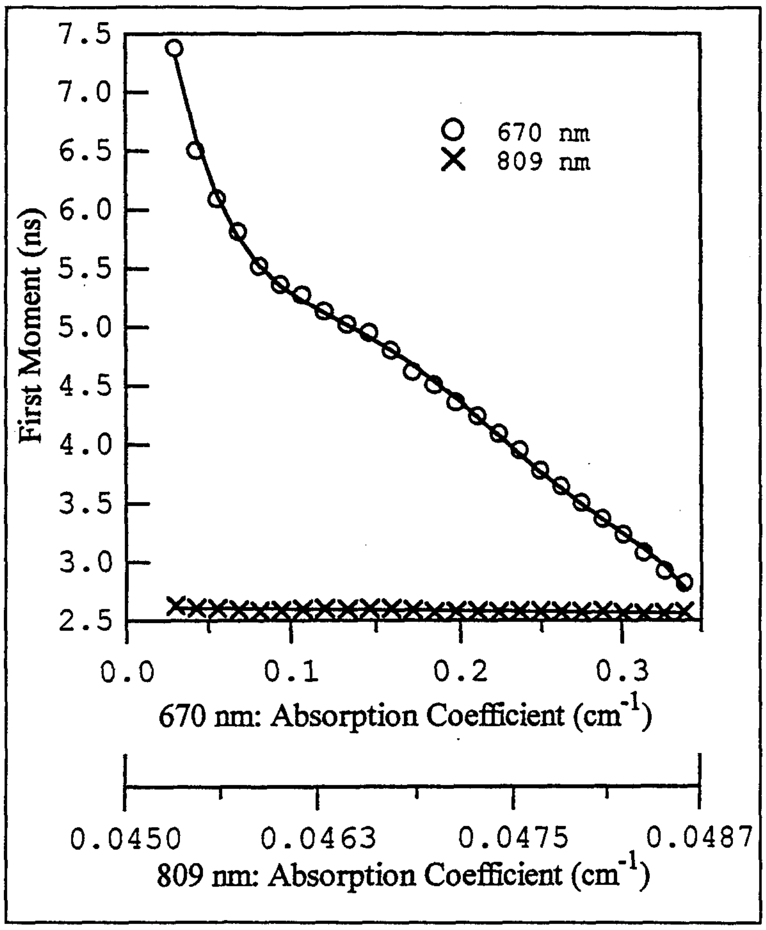

Figure 4.6. First moment of correlation vs. Absorption coefficient.

Monotonic decrease in the first moment from 7.4 ns to 2.8 ns is observed as the absorption coefficient increases, with a 670 nm transmitter. However, the first moment with a 809 nm transmitter remains almost constant at 2.6 ns with a maximum variation of 50 ps which is approximately the system resolution, over the wide range of ink concentration change. It is because the ink used in the experiment is relatively transparent at 809 nm light while highly absorptive at 670 nm. This result clearly demonstrates the effectiveness of the PRM method in a differential absorption measurement paradigm such as needed for deep tissue hemoglobin oxygenation. In this strategy two wavelength measurement will be implemented using two orthogonal pseudo random codes. The wavelength pair will be chosen one at isobestic point for hemoglobin absorption (~820 nm) and the other at a point with the maximum sensitivity to oxygenation (~690 nm or 760 nm). In this scheme, the 820 nm channel will measure the total Hb content and the 690 nm channel will measure the oxygenation of Hb. Since the absorption coefficient of the Hb is an order of magnitude higher than that of oxy-Hb, a very reliable measurement of the oxygen saturation with a few percent accuracy will be readily accomplished.

Figure 4.7 shows the normalized peak intensity as a function of the absorption coefficient.

At 670 nm, the variation in ink concentration leads to almost three orders of magnitude change in peak intensity. However, only 25% peak intensity change is observed at 809 nm since the same amount of change in ink concentration causes very small change in absorption coefficient, up to 0.004 cm^{-1} at this wavelength. While the peak intensity is a very sensitive indicator of absorption coefficient, it may not be a reliable parameter to be used in the field. External noise such as shock, vibration, interference E&M wave, or temperature variation could alter the intensity measurement results significantly.

ii) Reflection Measurement

Temporal pulse spread function (TPSF) of the PRM measurement depends on both the scattering and absorption coefficient. For a given scattering coefficient, the absorption coefficient will be decided accurately and uniquely from the simple functional relationship between the first moment and the absorption coefficient, without resorting to a complicated nonlinear algorithm. This offers a significant advantage for the battlefield operation or clinical emergency medical unit where trained medical personnel are not available. If the patient information for the normal tissue is available during the care, one measurement will provide the diagnosis, because the diagnosis (for hemoglobin and oxygenation change) requires the measurement of change in the absorption coefficient only. Nevertheless, if the normal tissue data is not available the sensor should provide capability of measurement for both absorption and scattering coefficient simultaneously. These two optical parameters influence the photon diffusion process in a complex manner such that it is not easy to retrieve one parameter independent of other.

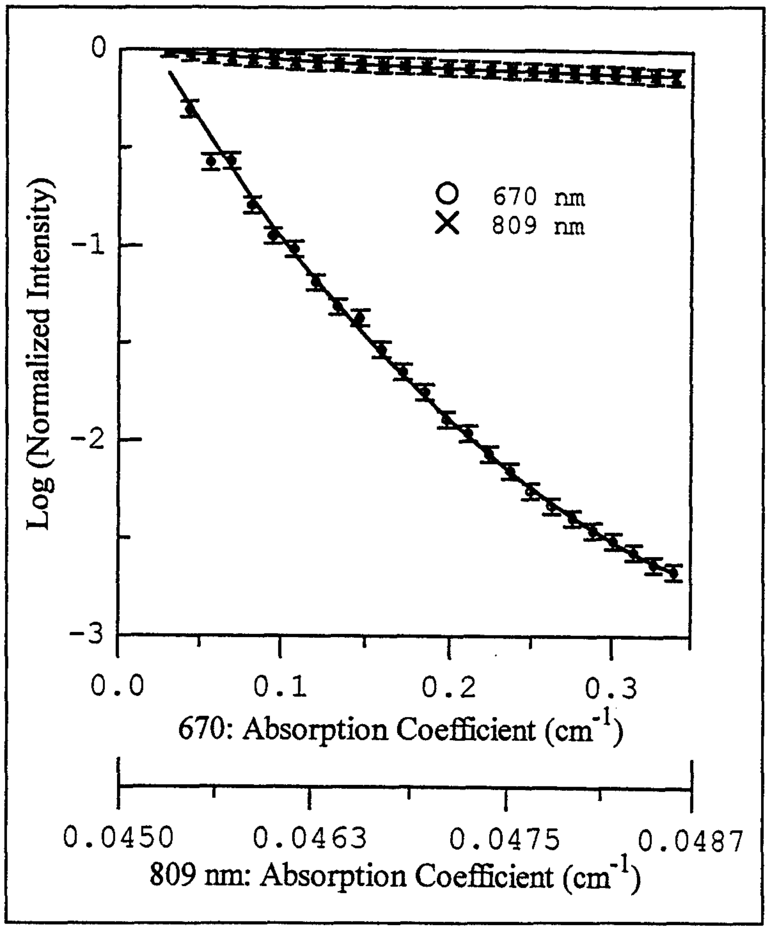

Figure 4.7. Peak value of the correlation coefficient vs. the absorption coefficient.

As discussed in Section 4.4, in our measurement the first moment shows different contours for different scattering coefficients. The contours obtained by the reflection

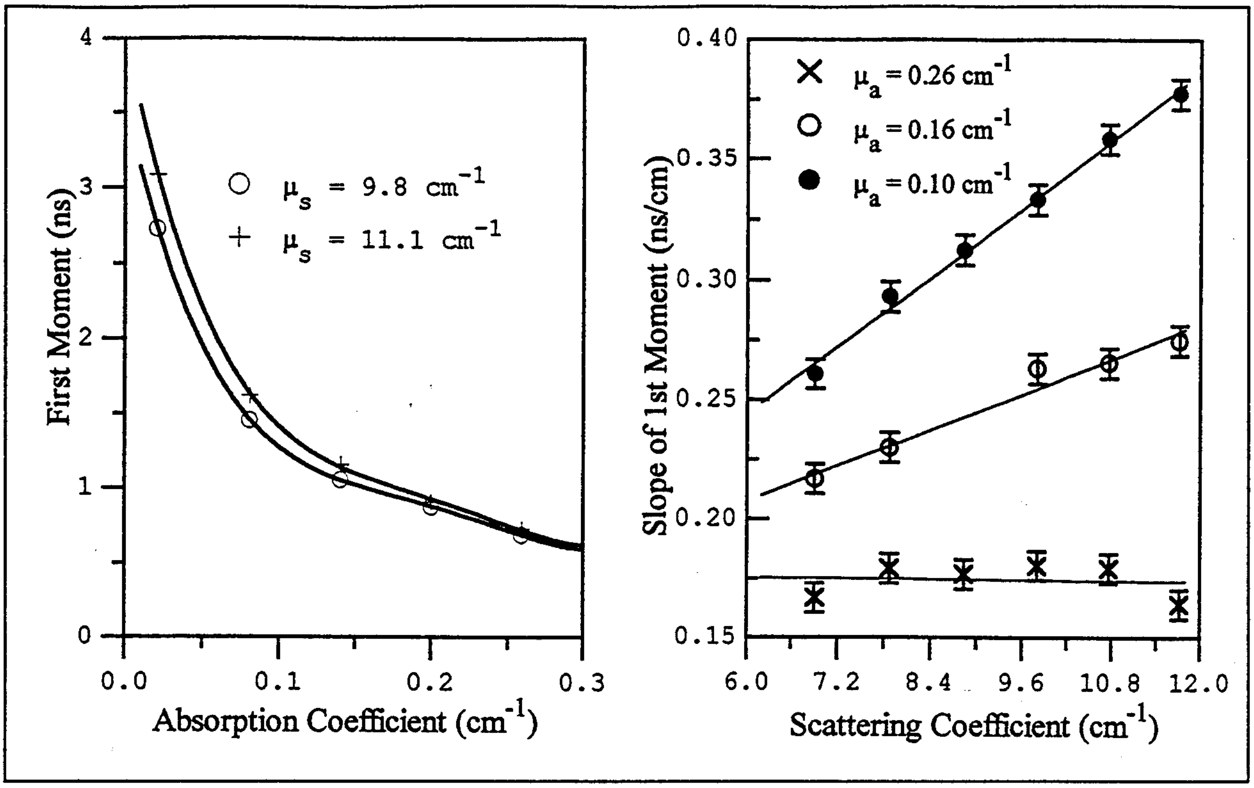

Figure 4.8. (a) Contour of first moment of the correlation coefficients as a function of the absorption coefficient for two different scattering coefficients (b) Slope of the first moment as a function of the scattering coefficient for various absorption coefficients. This data forms the basis of the simultaneous measurement of the optical parameters of the tissue.

measurement with an intralipid phantom is shown in Fig.4.8(a). The scattering coefficient was varied over 10% by changing the intralipid solution concentration. Although the two contour lines are relatively close to each other, they are significantly different. Thus the simultaneous measurement for absorption and scattering coefficient is required. A new and simple method to satisfy this requirement was considered during Phase I. This method is based on the alteration of the photon paths by changing the separation distance between the source and the detector. Fig.4.8(b) shows the differential slope of the first moment of the correlation over 2 cm and 6 cm separation. The slope contours for various absorption coefficient show monotonic increase as a function of the scattering coefficient over a wide range of the tissue parameters. This result, together with the functionality of first moment vs. absorption coefficient shown in Fig.4.8(a) provides a simple basis and a robust method for accurate and unique retrieval of the complete optical parameters of the tissue needed for hemoglobin and oxygenation diagnosis. In this method, no *a priori* information on the tissue is required. The measurement scenario would be: 1) measure the slope of the first moment from 2 cm and 6 cm separation data. Assuming a normal tissue absorption coefficient, obtain the scattering coefficient from the contour in Fig.4.8(b). Using this scattering coefficient read the absorption coefficient of the tissue from the contour in Fig.4.8(a). Now the first estimation of optical parameters can be further improved by iteration method using the same contour data until the successive estimation comes close within the error bound of the measurement. The last value from the iteration will then be used for hemoglobin concentration and oxygenation estimation.

4.5.3. Strong Absorber Depth Measurement

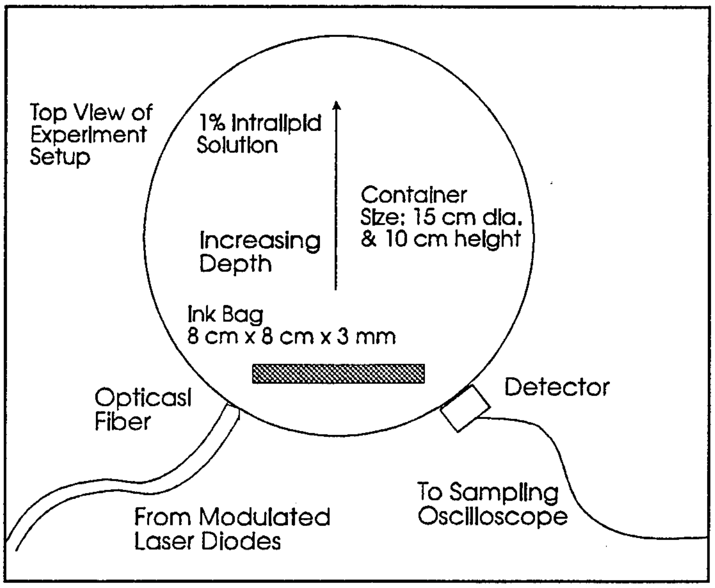

Figure 4.9. Schematic of experimental setup for absorber depth measurement.

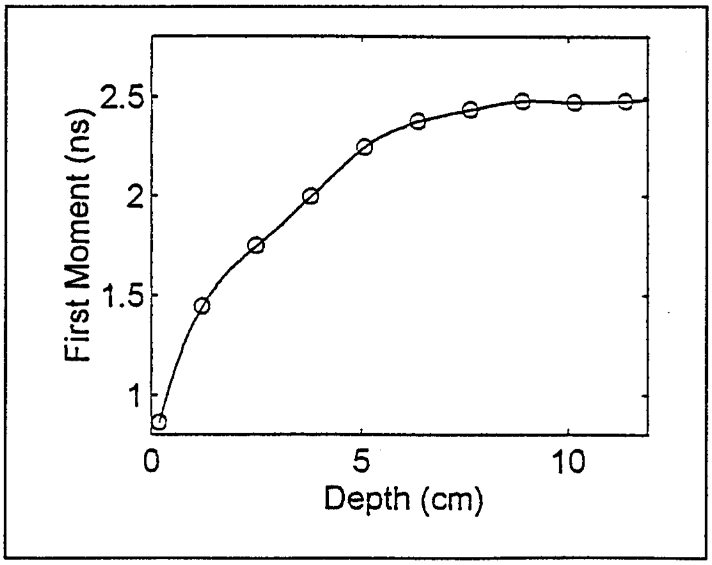

Figure 4.10. First moment of the ERF as a function of the absorber depth.

Deep tissue measurement requires a large penetration depth of the transmitter light as well as high time resolution of the system to differentiate the deep tissue signal from the strong surface return signal. The PMS system fails this requirement, no matter how strong the signal is, due to the lack of the time resolution, while other TRS methods with a picosecond laser are limited for the signal penetration depth due to the low S/N ratio. In contrast PRM/RET uniquely provides both the large signal penetration depth as well as high time resolution. In addition, the PRM/RET allows exact synchronization of the predicted waveform to the measured ERF, enabling a unique capability of the sensor for the accurate measurement of the maximum likelihood of pulse peak position. In order to demonstrate the large penetration depth capability of the PRM/RET, a simple simulation experiment was performed to detect the depth information of a strong absorption layer imbedded in a phantom solution. As shown in Fig.4.9, a thin layer of ink (3 mm) is located at various depths from the surface of a 0.5% intralipid phantom, and the first moment of the ERF is measured for each location. The result of this measurement shows a continuous increase in the first moment as a function of the depth of the absorber up to 8 cm level, as shown in Fig 4.10. This data clearly demonstrates an extremely large penetration depth of the PRM/RET measurement. Although the skeletal tissue optical density is somewhat higher than that of the phantom used, we estimate that a 3-4 cm penetration depth can be readily obtained based on the extrapolation of this data.

4.5.4. Measurement of Heterogeneity

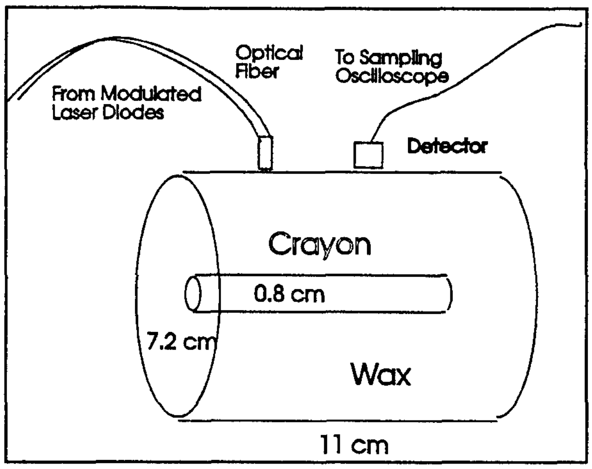

Figure 4.11. Schematic of experimental setup for single inhomogeneity measurement.

Further proof of concept experiment was performed using heterogeneous phantoms. As shown in Fig. 4.11, a solid cylindrical phantom (7.2 cm dia x 11 cm height) made of white wax is used to simulate the breast tissues. A cylindrical hole of 0.8 cm diameter is drilled at 1.6 cm off center parallel to the axis of the cylinder. Different kinds of

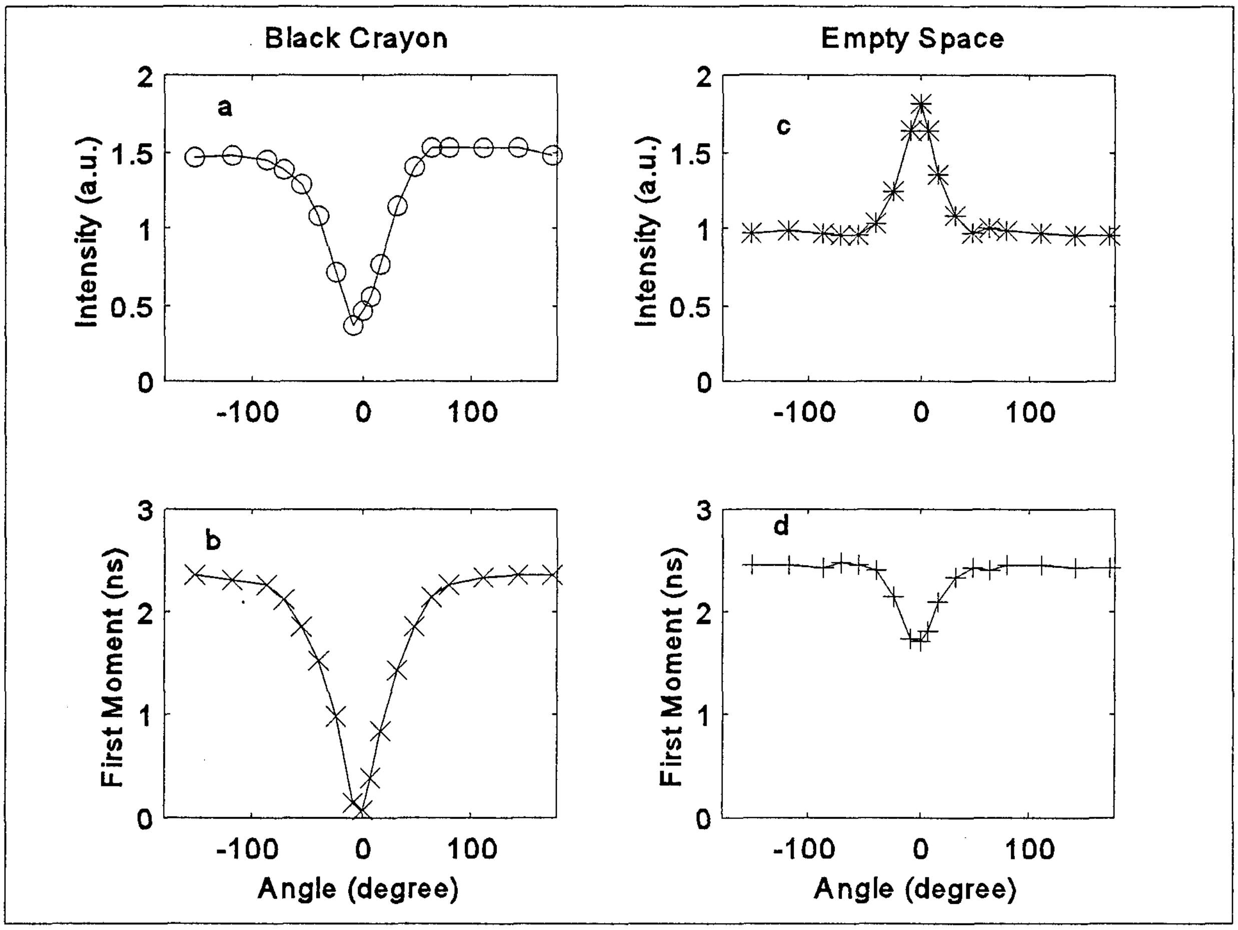

Figure 4.12. Intensity and First moment signature of heterogeneity in a diffusing media.

inhomogeneities are planted into the hole, such as crayons and empty space. The result of the experiment with this phantom is depicted in Fig.4.12. In this figure, the first moment of the correlation profile is plotted as a function of the laser beam/detector pair location relative to the position of the absorber imbedded in the off-center axis of the cylindrical shape phantom. Remarkable sensitivity of the first moment to the absorber is clearly demonstrated by the large change (order of a few nanoseconds) in the first moment by the presence of the absorber. The signature of the heterogeneity is revealed by the sharp change in the first moment and intensity right above the absorber with a significant magnitude compared to the measurement accuracy of a few tens of picosecond. The observed spatial resolution is well explained by the photon diffusion in the phantom.

4.6. Summary of Phantom Measurements

The Phase I data indicate the robust performance of the PRM/RET for deep tissue diagnostic applications.

- The phantom measurements defined the intrinsic accuracy of the breadboard PRM/RET measurement at a level of 0.001 cm^{-1} for the absorption coefficient and 0.07 cm^{-1} for the scattering coefficient, respectively.

- A simple and robust method for application of PRM/RET data was developed and utility of the method was demonstrated based on the first moment (of the correlation profile) and the slope of the first moment for different separation distances (between the source and the detector).

- Differential absorption measurement capability was clearly demonstrated using 670 nm and 809 nm. Furthermore, the deep penetration depth (8 cm) of the PRM/RET measurement was directly demonstrated in a phantom representing a soft tissue.

- The PRM/RET was further tested to demonstrate the capability of detecting the heterogeneity imbedded in a deep tissue like phantom.

5. Prototype System Design

The two main elements, transmitter and the data acquisition system, will be integrated into physically one unit. At the same time the design should keep the system as modular as possible. The modularity gives more flexibility during the development of the final system and helps in the final integration process.

Before the design of the final, highly integrated PRM sensor we plan to experiment two intermediate prototype devices. The first prototype is an intermediate integration, where the moderate speed electronics are integrated into high density programmable logics. The PRM sensor electronics probably takes up to 3 x 10" x 10" printed circuit boards. First board is the signal generator with the laser diode driver. Second board the analog input, digitizer, arithmetic and logic unit (ALU) and data memory. Third board is the timing, sequencing, control and computer interface. The boards have to be "sandwiched" together to maintain the high speed and timing precision. Adding power supplies and proper cooling to the electronics, it can be built into a conveniently transportable and easy-to-handle instrument box. This box will be connected to a desktop computer and used for laboratory experiments.

The next version prototype will be developed for portable applications. The computer (as embedded computer) will be added to the electronics box as the 4th board and integrated into the instrument box. A human-computer interface will be developed (display and control keyboard) according to the specific application. The final electronic integration will assure minimum size and cost of the system.

5.1 NIRS PRM Sensor Laser Transmitter

Two main elements of the transmitter module are the PRM code generator and the laser diode driver circuits.

PRM Code Generator

In Phase I of the project two types of PRM code generators were designed and built: a 200 MHz modulation frequency generator (200PRM) and a 400 MHz modulation frequency generator (400PRM). The 200PRM is a single channel signal generator with an external trigger generator requirement and computer selectable code length capability. The 400PRM is a dual-channel signal generator with an internal trigger generator and with an independent jumper-selectable code length for each channel. The trigger frequency is computer selectable.

The tests of the two PRM generators proved the validity of the circuit design. The final version of the PRM code generator will be based on the 400PRM. The use of custom (or semi-custom) design ECL chips (e.g. Synergy SY1BP00 - SY34BP00 family) allows us to realize 400 MHz modulation frequency generator with computer selectable code length. The present 400PRM, built from standard ECL logic circuits, could reach the 400 MHz modulation frequency only without the multiplexer needed for the computer selectable code length option. The custom design chip has shorter propagation time than the standard circuits and the external connections between the circuits can be completely eliminated. These two factors reduce the loop delay sufficient to add multiplexer to the 400PRM for computer selectable code length. Lower modulation frequencies can be also selected by the computer.

One additional advantage of using the Synergy custom design ECL circuit family for final integration is the built-in ECL-TTL converters. The computer control logics are naturally built from TTL circuits and the ECL and TTL connection surface always requires logic level converters in both directions. The Block diagram of the final PRM code generator is shown in Fig. 5.1. In the final integration of the PRM sensor electronics we plan to place a part of the timing electronics of the data acquisition system into the PRM generator custom chip.

Laser Diode Driver

The highest modulation speed of the laser diode current requires a balance between the DC and AC components of the diode current. The DC component is called bias current and the AC component is called modulation current. The planned diode driver has to be able to deliver at maximum 250 mA bias and 300 mA modulation current. The present laser diode driver with some modification could deliver these currents. However it is built from discrete components and thus incompatible with our integration effort.

ECL logics integrated laser diode driver circuits are available in the market. SONY has a chip (CXB1108Q) with 60 + 60 mA currents (bias + modulation) and 2 Gbps (Giga bit per second) maximum modulation frequency. Hewlett-Packard also has a driver chip (IDA-07318) with 50 + 50 mA currents and 1.5 Gbps maximum modulation frequency. Obviously any of these chips has much lower current capability than what we need. We are planning to make an experiment to connect together in parallel as many

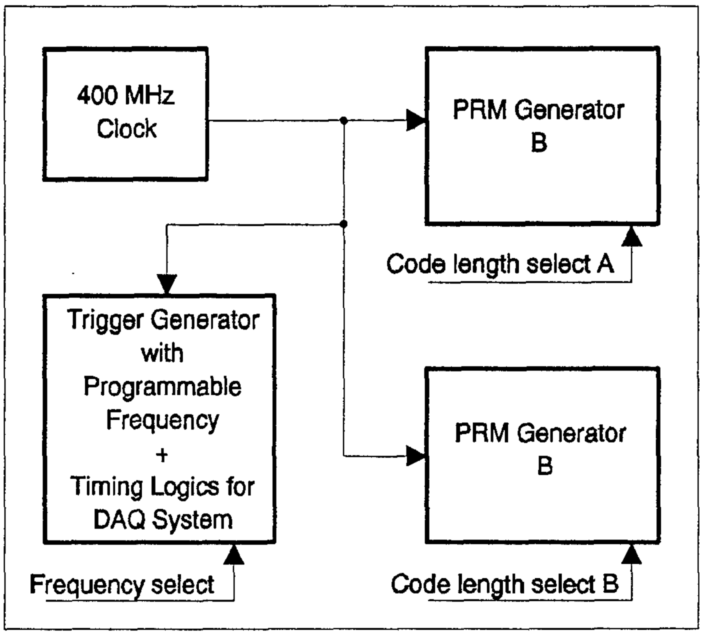

Figure 5.1. PRM code generator.

chips as it necessary to reach the required current values (5 or 6 chips). The parallel connection of these chips is doable because each of them can sink only a given amount of current, so the current division between the chips is automatic. A possible arrangement of the laser diode driver from parallel connected chips can be seen in Fig. 5.2. The real problem is the effect of the different propagation delays of the different chips plus traces on the printed circuit board. The propagation delay uniformity is not specified for the chips, it has to be checked experimentally. The trace delay uniformity is a problem associated with the circuit layout design and construction thus can be only tested experimentally. The difference of the shortest and longest total propagation delay can not be larger than the rise time of the driver output (~200 ps), otherwise the expected single transition becomes a multiple step transition with significant rise time degradation. The transition in the excitation laser beam should happen within as short time as possible. If the experiment with the parallel connected driver chips gives acceptable or near acceptable result, we can integrate the driver chips into the PRM code generator custom designed ECL chip. Shorter interconnection lengths and more uniform elements in the custom chip will improve the propagation delay uniformity. If the design does not give positive result, we will design a separate laser diode driver from discrete elements similarly to the present one.

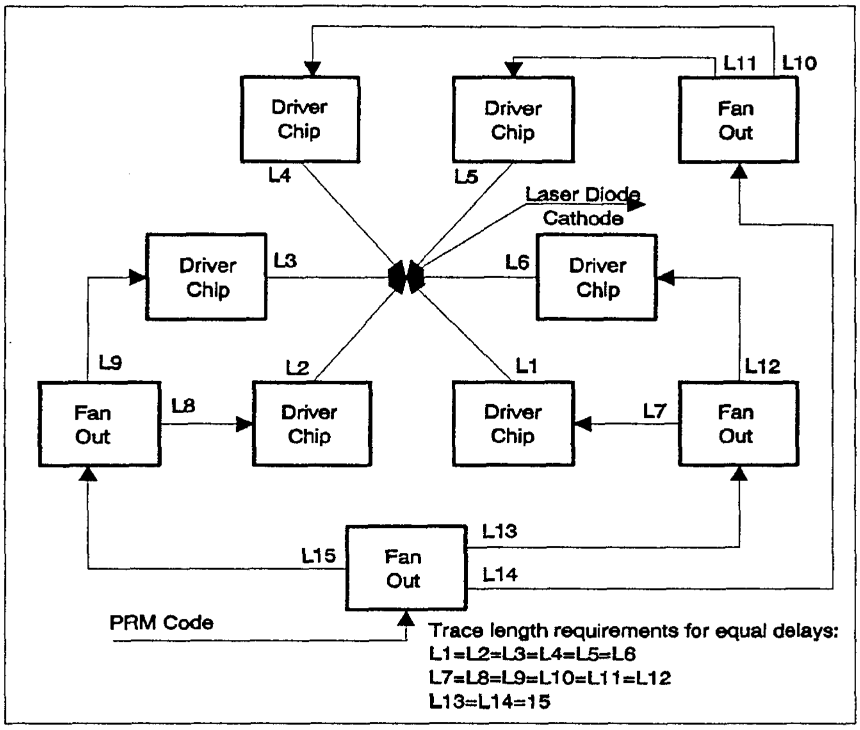

Figure 5.2. Laser diode driver with integrated driver chips.

5.2. Data Acquisition System for NIRS PRM Sensor

The basic requirements for the PRM sensor Data Acquisition System are:

- It must be moderate in size and cost considering the requirement for portability and the large volume production.
- It has to be flexible enough to fit into different applications easily and to accommodate different level of processing complexities (Interfacing capability to embedded, notebook and desktop computer without significant modification).

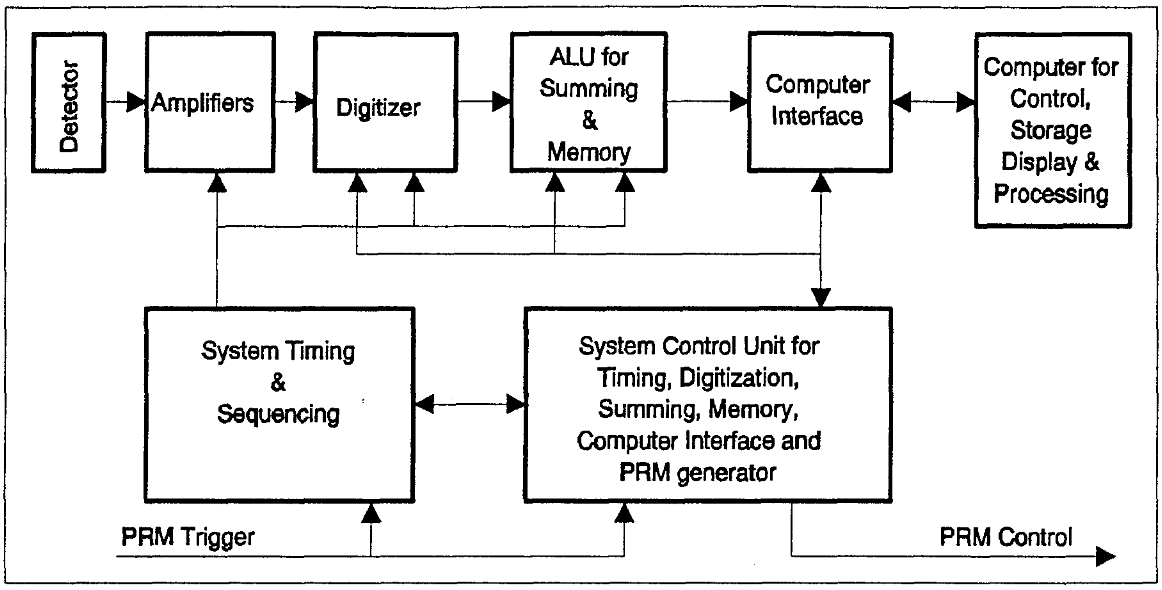

Figure 5.3. Data acquisition system for NIRS PRM sensor.

- The analog bandwidth has to be above 1 GHz.
- The aggregate sampling rate has to be around 20 Gsps or higher.
- The circuit elements of the system has to be integrated to the highest possible degree using programmable and custom designed integrated circuits.
- The computer interface has to have a standard surface toward the computer and this standard has to be available for embedded, notebook and desktop computers.

The block diagram in the Fig. 5.3. shows the schematic of the data acquisition system. The analog elements are the amplifiers and the digitizer. The remaining parts, the ALU, memory, computer interface, timing and sequencing and the system control, are digital elements. Due to the high speed, the ALU and some part of the timing and sequencing have to be built from ECL logics. The following part gives detailed description about the elements of the data acquisition system.

Amplifiers

In the ideal case the detector delivers large enough amplitude signal to the ADC (digitizer) without additional amplification (Fig. 5.4.a.). This solution has the largest bandwidth because the limitation of the amplifier does not affect the design. Although the single shot sampling rate is designed for only 100 Msps, we have to use higher bandwidth ADC to achieve the necessary bandwidth (1 GHz). The ADC input range is 1 or 2 V.

Detectors with small output signal (10 - 100 mV) require amplifiers before the ADC (Fig. 5.4.b. and c.). At very high frequency the amplifier with gain larger than 5 generally is composed from multiple stages to maintain the high bandwidth. In the PRM system the amplifier has to have high slew rate, in addition to the very wide band, because the ADC input requires at least 1 V signal. For example Analog Devices and Burr Brown have several amplifiers with high slew rates (>2000 V/s) or high bandwidth (> 3 GHz gain bandwidth). The selection of the proper amplifier will be possible only after the selection of the detector and ADC. Tradeoff design between the bandwidth and the slew rate requires further study. In our case we have to balance out the two parameters for high speed pulse amplification with minimal distortion.

We have to be very cautious about using flash ADC without Track&Hold amplifier because the high slew rate signal can cause extremely large digitization error (Fig. 5.4.b.). An alternative solution can be seen in Fig. 5.4.c., where a Track&Hold amplifier is placed in front of the ADC. The detailed explanation of the use of T&H amplifier is discussed below.

Digitizer

At present the commercially accessible highest speed 6 or 8 bit precision ADCs with reasonable price have around 1 Gsps digitization rate. For this reason the 20 Gsps digitization rate with the above precision can be achieved only by repetitive sampling method. This method requires repetitive signal with stable amplitude and phase. Luckily our signal is repetitive and stable enough to be digitized with this method.

The repetitive sampling method uses a gradually delayed digitization clock. The delay step is equal to the time between the samples. The actual single shot digitization rate can be quite low if the signal quality allows it. The following factors have to be considered when the single shot digitization rate is selected for repetitive digitization method:

- Higher single shot rate results higher efficiency and shorter measuring time. In our case the increased measuring time is not critical, with 100% efficiency the measuring time would be around 5 ms.
- Low single shot rate can be handled by low speed, cheaper logics and memory. Exception is the delayed digitization clock generator, because the stable highly grained delay requires high speed logics.
- As the single shot rate goes low, the clock generator and the control logics become more complicated due to the large number of delay steps (e.g. at 1 Msps single shot rate 10,000 steps is required to reach the 10 Gsps repetitive rate or sample density).
- The lower is the single shot rate the larger is time in the original signal the adjacent samples of the sampled signal. The low sampling rate decreases the fidelity of the sampled signal. Our measurement uses an average of large number (up to several thousand) of sampled signals, so the single signal fidelity is not so critical. For averaging many signals, the repetitive sampling method works quite well.

Based on the tradeoff design, we consider a 50 - 100 Msps single shot digitization rate in our case. As mentioned before the input bandwidth of the ADCs is directly proportional to its sampling rate. For example the Signal Processing Technologies SPT7710 8 bit, 150 Msps ADC has only 210 MHz input bandwidth. Higher input bandwidth relates to higher sampling rate. The SPT7610 6 bit 1 Gsps ADC has 1.4 GHz input bandwidth, the SPT7760 8 bit 1 Gbps ADC has 900 MHz input bandwidth. We plan to use one of these ADCs with 100 MHz clock rate only. These large bandwidths are useful only if nothing limits them between the detector and the ADC. It is definitely the case in Fig. 5.4.a. As soon as we have to use amplifiers, the bandwidth will be limited. The actual bandwidth (definitely above several hundred MHz) can be decided only after doing experiment with the real signal, because we have to balance the bandwidth and slew rate to gain the highest sensitivity of the PRM probe system with a given signal processing method.

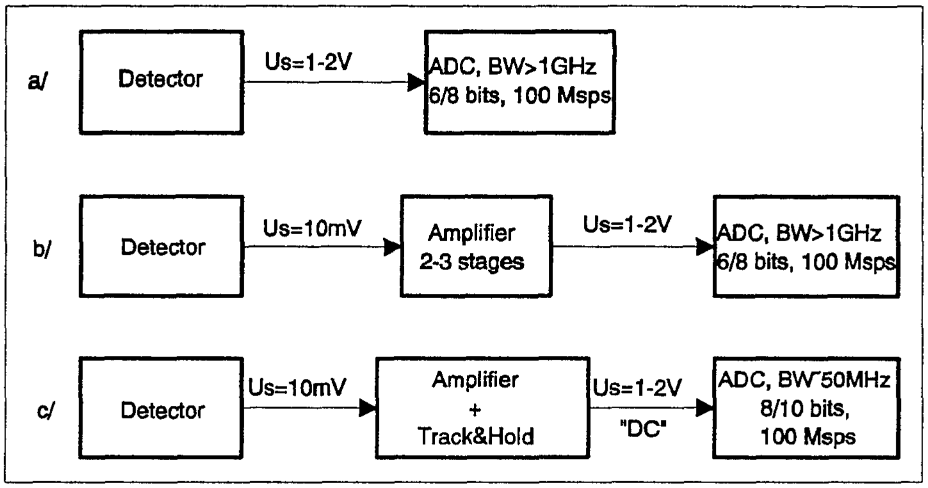

Figure 5.4. Possible analog input arrangement.

Using Track&Hold (T&H) amplifier as one of the stages just before the ADC offers a different approach to the analog part of the data acquisition system (Fig. 5.4.c.). The T&H amplifier or sampling amplifier has an additional digital control input. When the control input is in one state, the output of the sampling amplifier follows the input. When the control the transition happened. Analog Devices has a sampling amplifier (AD9101) with 350 MHz sampling bandwidth and 125 MHz sampling rate. The slew rate and bandwidth of the sampling amplifier are balanced out for large signal (analog digital conversion) application. The sampling amplifier eliminates the large bandwidth requirement for the ADC and allows the use of a real 100 Msps ADC. In the future probably a better sampling amplifier will be available as the sampling rates of the flash ADCs increases. Other alternative is to use custom designed input amplifier with sampling stage. The feasibility of these amplifier is proved by the latest digital sampling oscilloscopes from Tektronix and LeCroy. There is one more supporting fact to use sampling amplifier in front of the ADC. The high slew rate signal can significantly increase the digitization noise in the flash ADC without T&H.

We propose to test both versions (Fig. 5.4.b. and c) of the digitizer and select the better performing one in our environment. The 1 Gsps ADCs have dual, demultiplexed outputs. (Unfortunately the 8 bit resolution ADC outputs are grey coded and it makes its application more difficult for us.) The demultiplexed outputs (output bank A & B) help to implement an alternating pipeline service at the outputs. Although the dual output requires to double some of the service circuitry, it allows us to use slower (and cheaper) logics at the same ADC sampling rate. The 100 MHz ADC has only single ECL output, and for this reason it requires external demultiplexing logics to establish dual bank output.

Summing ALU and Data Memory

The block diagram of the unit can be seen in Fig. 5.5. The dual bank (demultiplexed) output of the ADC extends the service time of the outputs at the expenses of the logics complexity. Because the speed and price are not directly proportional, the realization of the same function by using more complex but slower circuit can be cheaper. Additionally, above certain speed limit the feasibility itself becomes questionable. In our case the dual bank output of the ADC allows 20 ns service time per output instead of 10 ns. Even if we consider all other functions fully pipe-lined with the memory RD/WR functions, the 5 ns range for RD/WR would require very expensive memory. Memory chips with 10 ns RD/WR times (dual bank output) are significantly cheaper. For this reason at single output ADCs (100 Msps) it is reasonable to add the logics externally to demultiplex the output.

The nature of the measurements with the PRM sensor requires to average the input signal patterns up to several thousand. To store several thousand patterns and average them later means huge memories at the planned (20 Gsps) sampling rate. The signal-by-signal transfer and averaging would slow down the measurement almost to unbearable extent. The

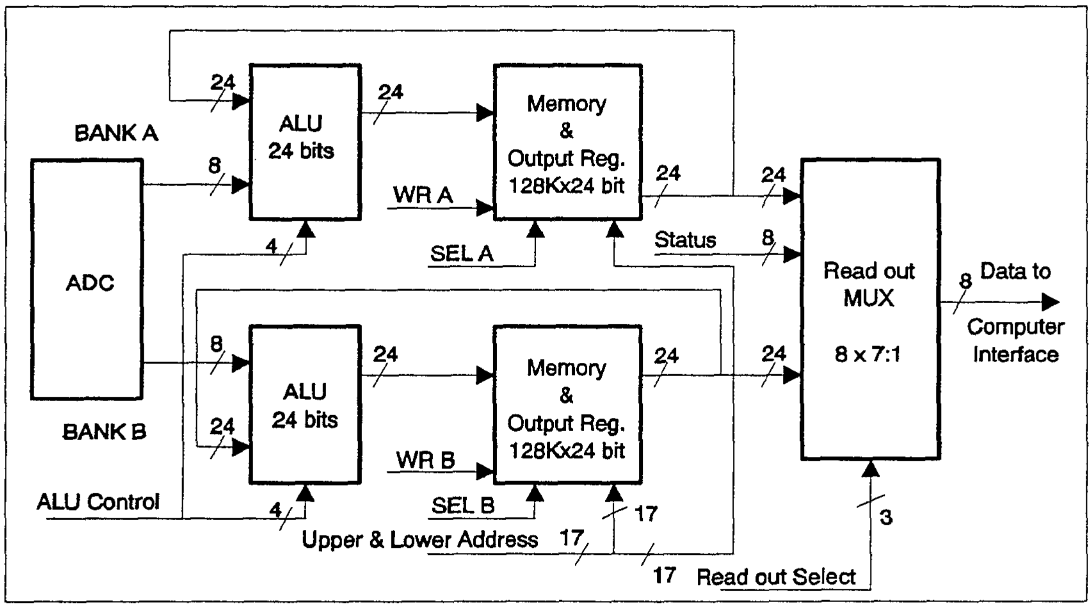

Figure 5.5. Summing ALU and data memory.

straightforward choice is to build the averaging process into the data acquisition hardware. The most time consuming part of the averaging is the summing. We selected the summing process to build into the DAQ hardware. The simplest realization of the summing logics uses ALU (Arithmetic and Logic Unit) chips. The 24 bit wide ALU design can sum up to 65,000 8 bit or 16,000 10 bit binary numbers. With ECL ALU elements one addition requires ~5 ns. (The finishing part of the averaging, the division, requires floating point calculations and can be done in the computer much more effectively.)

The data memory size can be calculated from the PRM code length, clock frequency and the ADC repetitive sampling rate. 1024 bit PRM code with 200 MHz clock frequency and 25.6 Gsps sampling rate requires 256 K x 24 bit size memory for storage.

The sequence of the data read out from the ADC and storage into the memory is the following:

- Read out the previous sum from the memory and feed it into the ALU as one of the two terms.
- Feed the ADC output into the ALU as second term.
- Wait until the new sum appears at the output of the ALU.
- Write back the new sum into the memory.

To execute this sequence within 20 ns with ~10 ns cycle memory and ~5 ns ALU (the plain sum of the times is 25 ns) requires pipeline operation of the summing loop. The pipeline operation in this case means to execute the addition during one of the memory operation (RD or WR). The pipeline design technique is well-known and common method to decrease the cycle time in complex systems.

The read out of the acquired data from the data memory into the computer takes place through 8 bit parallel port. The read out multiplexer divides the 2x24 bit outputs of the memories into six 8 bit wide segments and an additional 8 bit segment is used to transfer the status information. The multiplexer, during the read out, is used as a tool to organize the transferred data into proper order in the computer. (The dual bank handling of the ADC output saves the consecutive sampled data points into different memory banks.)

Computer Interface

The selection of the computer interface based on the following criteria:

- The computer side of the interface must be standard and simple.
- The same connection surface should be applicable to connect to desktop, notebook and embedded computers. The criteria limits the possible choices. Our choice is the National Instrument standard I/O connection. For PC AT and notebook computers the company sells

pin compatible I/O interfaces. Both interfaces are based on the Intel 8255A Programmable Peripheral Interface chip. Because of the general acceptance of this I/O chip, the availability of it in embedded computers is standard. For driving and isolation purposes driver and receiver circuits are used in the computer interface part of the data acquisition system.

System Timing and Sequencing

The correct and stable timing of the data acquisition system is extremely important. The desired sampling rate is 25 Gsps. At this rate the time interval between the sampled data points is 40 ps (picosecond). We have to maintain this level of stability in the system to be able to use the benefit of the very high repetitive sampling rate. As it was mentioned before, the 25 Gsps rate is possible only by repetitive sampling. The actual measuring time (summing several thousand sampled signal) will be around a second with this method. This time is short enough to consider the examined process constant.

The principle of the repetitive sampling is fairly simple. We would like to sample a repetitive signal in every "t" second, but we have only possibility to sample it in every "T" second, where T = N x t and N > 1. Let us assume N=10. First we start the sampling at the beginning of the signal (at the trigger) and take samples in every "T" seconds. When the signal begins again we start the sampling at "t" time (relative to the trigger signal) and take samples after every "T" seconds, that is we delay the sampling clock with "t". At the next beginning of the signal the sampling clock will be delayed by "2 x t". We repeat this process until we reach the "(N-1) x t" delay after N repetition of the signal, and we have a set of samples of the signal which correspond to "t" second period sampling but was taken by "T" period sampling only. The principal design of a timing circuit which deliver timing and sequencing signals to the sampling and storage circuits can be seen in Fig. 5.6.

In our case it is very important that the PRM Trigger signal is synchronous to the 100 MHz clock from the PRM Generator. Otherwise the sampling clock has to be synchronized to the trigger signal (to the beginning of the signal), which is not an obvious and cheap task.

The Phase Splitter Delay Line serves only a source of multi-phase timing signals. The 100 MHz sampling clock goes into a Programmable Delay Generator, where it is delayed in 40 ps steps 256 times (actually only 250 steps are used: 250 x 40 ps = 10 ns.). The delayed output is used in the ADC to generate a sample. To store the samples in proper order requires the sequencer. The sequencer generates the memory address where a given sample is stored to and organizes this way the samples into proper order. The sequencer is set of counters: 1 bit Memory Bank Selector Counter (BS), 9 bits Memory Upper Address Counter (UAC), and 8 bits Memory Lower Address Counter (LAC). BS and UAC are cascaded and clocked by the 100 MHz sampling frequency, the LAC clocked by the PRM TRIGGER signal (beginning of the signal). The content of the Summing Counter (16 bits) is decremented after each finished sampled signal. The initial value is loaded from the computer and the data acquisition stops when the counter reaches zero (underflows).

The System Timing and Sequencing logics can be divided into a high speed part (Delay Line, Delay Generator, BS counter) and into a moderate speed part (the rest). The moderate speed part can be integrated into high density programmable logics (FPGA or PLD). The high speed part also can be integrated into the PRM generator clock logics assuming that the final solution of the PRM sensor electronics will be built as a single board, integrated unit.

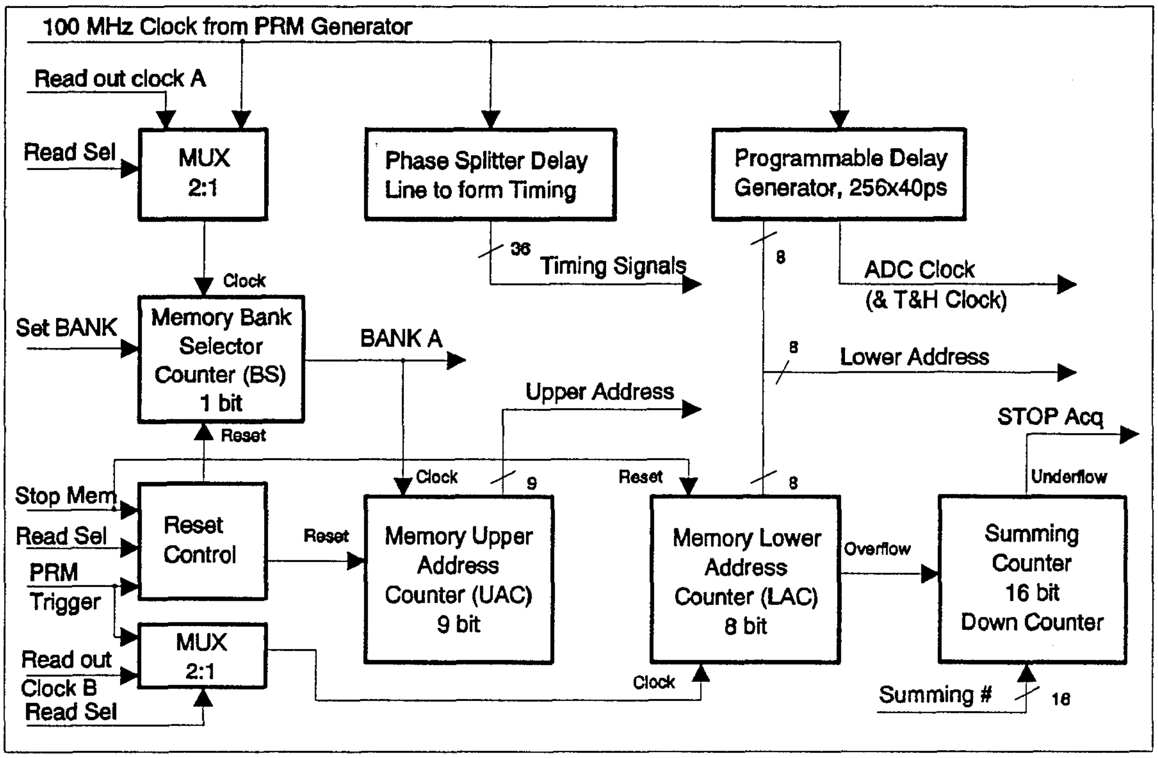

Figure 5.6. System timing and sequencing.

Control Unit

The PRM sensor electronics is too high speed circuitry to be controlled only by computer. It requires its own Control Unit which is set by the computer according to the function to execute. The selection and start of different functions in the PRM sensor is made by the computer and the execution is managed by the internal Control Unit (Fig. 5.7.).

Without giving a full list some of the PRM sensor functions are:

- Acquisition (single, continues, diagnostic).
- Data Memory read out.
- Test (memory, logics).

The first two functions are obvious. The test function at different levels of complexity is very important in all cases where the output information from a device can be the basis of an important human related decision. Considering the field application of the PRM sensor, the basic function test must be among the system test procedures.

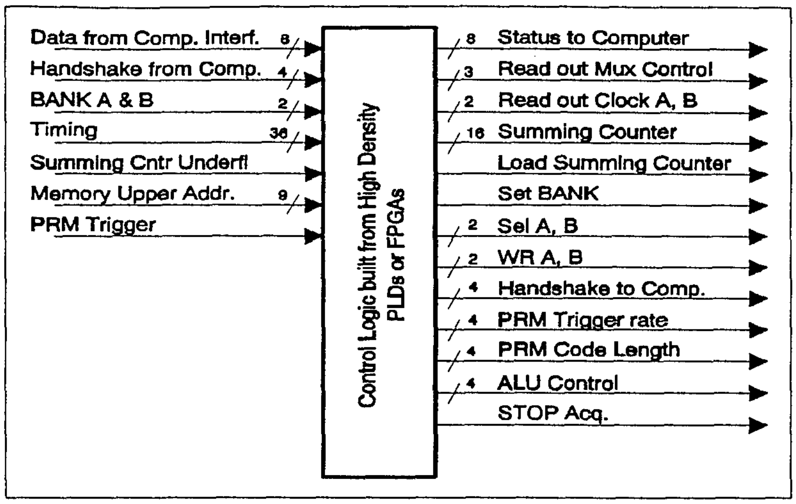

Figure 5.7. Control unit.

The realization of the Control Logics in the Control Unit can be done by using high density PLD or FPGA logics. The design of the state machines in the Control Logics is very convenient with the design tools supporting the PLD and FPGA programming.

5.3. Optical Interface

Optic fibers will be used for both transmitter and receiver end of the system. The laser output will be coupled to a multi-mode fiber bundle of a few millimeter diameter. The large beam divergence of the laser diode will matched to the throughput of the fiber by using an aspheric lens between the laser and the fiber tip. The fiber bundle size will be determined based on the acceptance angle of the fiber and matching the throughput of the diode output beam and the fiber. The collimating lens and fiber will be coupled directly to the diode laser using a fiber connector modules for a convenient assembly of the module. The receiver design will be performed in Phase II period for a fiber coupling between the sample and the detector. Since the signal from the sample is characterized by the diffused light, a Lambertian intensity distribution will be assumed, and the best light collection efficiency with a multi-mode fiber bundle will be achieved to maximize the signal.

In the proposed sensor application, the requirement for the spatial resolution is not very stringent and thus a relatively large size bundle can be used for the system. However, the time dependency of the received signal depends on the distance between the input and output point of the signal. Consequently the optical parameters derived thereupon will be also affected by the geometry, thus the size of the beam must be limited based on the required time resolution of the system. In Phase II, we will perform experiments to study the effect of the beam size on the signal in terms of its net effect on the optical parameter measurement. A maximum aperture size within the required measurement accuracy will be defined and implemented in the receiver fiber optic design.

6. Phase II Study Plan

6.1. Simultaneous Differential Absorption Technique

The novel simultaneous differential absorption technique to filter the tissue dependent false signal will be implemented using two wavelengths at 780 nm and 820 nm or 690 nm and 820 nm. Independent and orthogonal PRM/RET code will be employed for each wavelength to implement the truly simultaneous differential capability. The aim of this study is to optimize the wavelength pair selection in terms of filtering the time varying noise due to the total hemoglobin concentration.

Oxygen Saturation Calculation from Differential Measurement

Based on the unique characteristic of absorption spectra of the Hb and HbO_2 which give the same extinction coefficient at 820 nm, the two wavelength data may be effectively used to calculate the oxygen saturation quantitatively. Recognizing that absorptions by other components of the deep tissue are relatively small compared to the blood absorption and furthermore the monotonic spectra characteristics in this region [Yarborough, 1992], a set of linear equations with a perturbation term can be formed from the two measurements as:

$$\mu_a(\lambda_1) = \mu_a(\lambda_1)(Hb) + \mu_a(\lambda_1)(HbO_2) + \delta = \epsilon_{Hb}(\lambda_1)(C_0 - C) + \epsilon_{HbO_2}(\lambda_1)C + \delta$$

and

$$\mu_a(\lambda_2) = \mu_a(\lambda_2)(Hb) + \mu_a(\lambda_2)(HbO_2) = \epsilon_{Hb}(\lambda_2)C_0 + \delta$$

where ε is the extinction coefficient with the subscripts for component; λ_1 is a wavelength for large differential absorption signal and λ_2 is the isobestic wavelength for both components. C_0 denotes for the total hemoglobin concentration and C for oxyhemoglobin concentration. The perturbation term, δ, represents the additional absorption coefficient of the remaining tissues.

The solution of the linear equation with a negligible δ may be obtained for C_0:

$$C_0 = \frac{\mu_a(\lambda_2)}{\epsilon_{Hb}(\lambda_2)}$$

and for C:

$$C = \frac{\mu_a(\lambda_1) - \epsilon_{Hb}(\lambda_1)C_0}{\epsilon_{HbO_2}(\lambda_1) - \epsilon_{Hb}(\lambda_1)}$$

If δ is not negligible compared to the hemoglobin absorption, another wavelength measurement is necessary for the solutions of the equation. Here the melanin and water absorption around the spectral region is relatively wavelength independent, thus a very accurate solution is available. Implementation of three wavelengths in the PRM/RET instrument is very easy due to the mutual orthogonality of the PRM codes. A beam combination of the three wavelengths with different codes is all that required in this technique.

6.2. *In vitro* Measurement

In vitro study will be performed using a well quantified dynamic phantom model which will simulate various levels of hemoglobin concentration and oxygenation in deep tissues.

Dynamic Phantom Development

The goal of this task is to demonstrate that in a controlled environment, such as can be obtained using phantom models, the absorption coefficient, μ_a, can be accurately and reliably quantified. Given this can be done, we will then attempt to verify several potentially useful parameters that can be computed with knowledge of μ_a: hemoglobin concentration and hemoglobin oxygenation state (saturation (%Sat)). To achieve this task we will build a model similar to the Kurth/Chance phantom. This phantom consists of fine network of capillary tubing, the volume of which is known. The tubing can be perfused with varying compositions of oxygenated and deoxygenated blood at differing hemoglobin concentrations. By varying the composition of scattering materials surrounding the "vessels", the influence of light scattering on the ability to quantify hemoglobin saturation can be studied. The original model was designed to mimic the optical parameters found in head. To model muscle tissue we will add oxymyoglobin to the bathing medium in concentrations equivalent to those found in resting muscle [Whipple, 1926].

Because the model can be perfused with solutions of differing composition, hemoglobin oxygenation state (% Sat) can be changed independent of hemoglobin concentration. Light scattering within the field of illumination can be varied by altering the composition of the fluid bathing the inner fluid-containing tubing. We propose two experimental protocols.

Experimental Protocol A: These studies will demonstrate that in a field containing a scattering media optically similar to that present in skeletal muscle, $\mu_{a(800nm)}$ varies proportionally with hemoglobin concentration as the latter is changed over a physiologic/pathologic range (8 to 18 g/dl). The wavelength selected for monitoring is located near the isobestic point of dog hemoglobin (unpublished work performed at JHU/APL re: Spectral Absorption of Hemoglobin).

Experimental Protocol B: The saturation of the hemoglobin solution perfusing the phantom will be varied randomly by changing the amount of oxygen contained within the perfusing solution. Hemoglobin saturation will be determined by differential absorption spectroscopy using two wavelengths,

$$\%Sat \propto \mu a(\lambda 1)/\mu a(\lambda 2)$$

[Hielscher, et al., 1993; Haida and Chance, 1994]. It is important to note that the above equation contains a proportionality constant determined by both biologic and physical factors. Our initial efforts will focus on showing that the relationship between the ratioed variables and the independently measured hemoglobin saturation is linear. We will then characterize the proportionality as a means of achieving instrument calibration. Factors which may influence proportionality are instrument gain, types and kinds of laser diode used, and the construction materials of the phantom itself, as well as other absorbers contained in blood. An estimate of the biologic contribution will be gained in the preliminary studies.

Data Analysis: We expect to find that μ_a(800 nm) is linearly related to the hemoglobin content of the perfusate and that the slope of the relationship is equal to the millimolar extinction coefficient for hemoglobin ($\epsilon_{Hb(800\ nm)}$ = 0.21 $mM \cdot cm^{-1}$; [Van Assendelft, 1970]). We expect the relationship to be independent of the state of saturation of hemoglobin. Proportionality will be evaluated using regression analysis techniques. Statistically different slopes obtained in differing concentration or Hb saturation states will be tested-for [Goldstein, 1964]. Hemoglobin concentration and saturation state (the independent variables) will be measured using a Radiometer Heme oximeter (OSM-3). The potential problems we anticipate are related more with developing a uniformly perfused phantom, than with measurement of the stated optical parameters. This is because the "vascular" space within the phantom must be both relatively small in comparison to the "tissue" mass, and it should be uniformly distributed throughout the field of illumination.

6.3. *In vivo* Study

To examine the relationship between muscle hemoglobin saturation and the NIR spectral information, we will utilize a canine gracilis muscle preparation. In each dog a gracilis muscle will be exposed and freed of connective tissue. All blood vessels communicating with this muscle, except the major artery and vein and those vessels entering at the origin and insertion will be ligated. The obturator nerve will be severed and the distal end mounted on stimulating electrodes. The gracilis artery will be cannulated and perfused at constant flow by diverting femoral artery blood through a pulsatile pump. The gracilis vein will be cannulated and the venous blood passed through an extracorporeal blood flow probe before being allowed to drain into a collecting reservoir from which a pump will return it to the animal. Systemic blood pressure, gracilis vein outflow pressure, and blood flow will be recorded continuously on an 8-channel Gould chart recorder. Muscle vascular resistance will be computed as the ratio: $(P_a - P_v)/Q$; where P_a is arterial blood pressure in mmHg, P_v is venous outflow pressure in mmHg, and Q is blood flow in ml/min. Oxygen uptake by the muscle will be computed as $MO_2 = Q(Ca_{O2} - Cv_{O2})$; where Ca_{O2} and Cv_{O2} are the oxygen contents of the arterial and venous perfusates, respectively.

To produce muscle exercise the distal end of the sectioned obturator nerve will be stimulated using supramaximal 0.5-msec pulses at frequencies of 0.25, 0.5, 1, 2, 3, 4, and 6 Hz. At each exercise level anaerobic arterial and venous blood gases will be collected and analyzed on an ABL-3 blood gas analyzer and an OSM2 hemeoximeter.

To clarify the contribution of myoglobin to NIR absorption changes the muscle will be perfused for 20 minutes with oxygenated Krebs solution containing 0.35 mM ethyl hydrogen peroxide at 20 ml/min to convert myoglobin to the ferryl form and thereby prevent myoglobin desaturation [Tamura, et al., 1978; Whitburn, 1987; Wilson, et al., 1989]. At the end of the perfusion period the muscle will again be reperfused with blood.

To establish states of complete tissue oxygenation and complete tissue deoxygenation in vivo, respectively, we will perfuse the muscle with a Krebs solution containing 1 mM NaCN to bind the enzymes of the electron transport chain or with blood to which $Na_2S_2O_2$ has been added and then equilibrated with 95% N_2 + 5% CO_2 [Seiyama, et al., 1988].

Muscle hemoglobin saturation, (Sat_t), is dependent upon the balance between oxygen delivery (OD) and oxygen consumption. Experimentally, changes in Sat_t can be induced by altering either factor. OD (and hence, Sat_t) can be reduced by decreasing the partial pressure of oxygen in the arterial blood, decreasing the amount of hemoglobin in arterial blood, or by lowering blood flow. At constant arterial oxygen delivery, Sat_t is inversely related to oxygen consumption. Ideally, a sensor for measuring muscle tissue hemoglobin saturation would report this variable reliably, regardless of whether changes were induced by hypoxia (decreased oxygen in inspired air and hence lowered arterial hemoglobin saturation), vasodilation/ vasoconstriction (resulting in increased/decreased oxygen delivery relative to oxygen uptake), or exercise (increased oxygen utilization relative to oxygen delivery). However, because optically these types of stresses manifest themselves differently with changes in μ_a and μ_s, there is a firm believing that saturation computed from the (shallow) surface measurement will not correctly represent all conditions. The goal of this protocol is to validate spectroscopically measured Sat_t against venous Hb_{sat} in each of these conditions. **The goal of these studies is to test the hypothesis that muscle hemoglobin and its state of**

saturation with oxygen can be quantitatively measured *in vivo*. To this end four protocols will be performed. Protocol 2A addresses the question: Can hemoglobin saturation be determined quantitatively and independent of muscle hemoglobin concentration, blood volume, and metabolic state. Protocol 2B is designed to determine contributions of myoglobin to the optical signals. Protocol 2C evaluates the depth of light penetration into skeletal muscle and contribution of reflected light originating from depth to the overall hemoglobin saturation calculation.

Protocol 2A. Hypoxic-hypoxia versus anemic hypoxia: In 5 anesthetized, paralyzed dogs, $(Sat)_t$ will be varied by controlling the fractional amount of oxygen in the animal's inspired air (FiO_2). Six levels of hypoxia will be induced. Following a brief rest period the animal will be made anemic by incremental hemodilution with lactated Ringers solution. An example protocol proceeds as follows. Hypoxic-hypoxia will be induced by ventilating the dog with 21%, 15%, 12%, 10%, 8%, and 6% O_2 (balance nitrogen) breathing mixtures. At each level blood gases will be collected to ensure arterial hemoglobin saturation is stable, then a sample pair will be drawn for arterial and venous blood gases. Hemodynamic and PRM/RET measurements will be collected. The animal will be returned to room-air breathing for a 30 min equilibration period. Then an intravenous infusion of lactated ringers solution will be started. Paired arterial and venous blood gases and PRM/RET measurements will be collected as arterial hemoglobin concentration decreases.

Protocol 2B. Exercising skeletal muscle: After control measurements at rest, the obturator nerve will be electrically stimulated at increasing frequencies. At each level arterial and venous blood gases will be collected and PRM/RET measurements made. A 30 minute equilibration period will then be invoked in which the muscle is allowed to relax. The muscle will be perfused with hydrogen peroxide to convert myoglobin to its ferryl form and the stimulation procedure repeated.

Protocol 2C. Localized depth stimulation: A stimulating electrode made with multiple concentric rings located at periodic lengths along its long axis will be inserted into the body of the muscle between the light emitting and light collecting devices. By selecting pairs of adjacent electrodes along the axis and applying a controlled electrical stimulus, we anticipate being able to create regional changes in oxygen consumption within the body of the muscle at differing distances from the muscle surface. As the hemoglobin within these areas unload oxygen to fibers with elevated oxygen demands, a regional area of density will result. By evaluating the manner in which the TPSF is affected, we will be able to determine if localized deep tissue changes are capable of being measured in this tissue.

Protocol 2D. Two component measurement: In order to test deep penetration capability of the measurement and accurate assessment of the deep tissue states, we propose to perform two component measurement with animal model. For given condition an additional layer of the different optical properties will be introduced between the model and the PRM sensor. By varying the layer optical properties, the measurement performance will be assessed in terms of accuracy and penetration. Limitations of measurement and systematic bias will be tested and related to the clinical applications.

Data Analysis: Spectroscopic tissue hemoglobin saturation will be computed using the same procedure as described in Task 1. This value will be plotted against venous hemoglobin saturation and a correlation procedure applied to derive the coefficients of correlation. We expect to find that the same relationship is upheld, irrespective of whether venous hemoglobin saturation is altered by changing arterial oxygen partial pressure, arterial hemoglobin concentration, or by increasing tissue oxygen uptake. Also, we do not expect to find a difference between the plotted relationship between venous hemoglobin saturation and tissue hemoglobin saturation made before and after conversion of myoglobin. Our rationale for this expected result is that at the levels of stress applied, we do not expect myoglobin deoxygenation to occur. This result would be consistent with other reports in the literature [Seiyama, et al., 1988; Wilson, et al., 1989].

6.4. Clinical Pilot Study Design

Based on the *in vitro* and *in vivo* test results using the realistic model for deep tissue and the improved functions of the PRM instrument, a detailed clinical pilot study will be designed. The precise clinical application requirements for the PRM instrument will be defined based on the information regarding the epidemiology and treatment paradigm of the clinical patients. The study objectives will be defined to satisfy the statistical significance of the study results as well as requirements of the correlative diagnosis by other instrument modalities. A specific plan will be developed at Johns Hopkins University where Dr. Hanley, the Co.I. is affiliated. An Investigational Device Exemption (IDE) will be applied to Hopkins Hospital IRB for the clinical pilot study which will immediately follow the proposed project.

PRM/RET Sensors in clinical/battlefield applications

We propose to develop the PRM/RET method as a modular sensor that has capabilities for measuring NIR hemoglobin saturation from underlying deep tissues in humans. Because the physiologic applications are organ specific and will potentially include oxygenation under normal and pathologic function we have selected critically ill patients as the target population to consider in designing the sensor. This group of patients represents an invasively instrumented group of humans that as a matter of clinical practice undergo oxygen metabolism assessments. A group of consultants familiar with all aspects of physiology of critically ill, wounded and normal patients has been assembled. This group includes Andres Salazar of the Jackson Foundation, Cmdr. Brain Kelly Director of critical care USN, Bethesda Naval Research Hospital, and Geoff Ling Director neuro critical care US Army/Walter Reed Army Medical Center. Along with Dr. Hanley, they represent a unique working group of physicians with experience in military applications of medical and physiologic measurements including Dr. Salazar (penetrating missile injuries, Vietnam head injury study), Dr. Kelly (critical care, multi organ failure), and Dr. Ling (trauma, brain physiology, intracranial pressure elevation). The group represents a study committee of the NACABI Consortium, which is prepared to apply deep tissue O_2 sensors to clinical problems in the ICU setting when a suitable human monitor is developed.

Several potential investigations are possible depending on final penetration depth and ability to resolve two differing saturation compartments. These include noninvasive detection of brain SvO_2, Assessment of muscle SvO_2 during rest and exercise, multiple organ SvO2 measurement during hypotension and detection of high and low concentrations of hemoglobin. This latter goal is currently under direct evaluation in the clinical domain at Johns Hopkins University where Drs. Hanley and Wilson (with IRB approval) are investigating the ability of NIR to detect tissue hemoglobin in patients undergoing evaluation in the emergency department.

7. Conclusions

A breadboard NIR sensor system has been developed based on the novel Pseudo-Random Modulation/Resolution Enhancement Technique (PRM/RET) and using a medium power diode laser system. This breadboard system was used for time resolved spectroscopic (TRS) measurements of photon migration in a phantom model closely resembling a soft tissue. Analysis of the data from this measurement clearly demonstrates the unique capability of the PRM/RET sensor for accurate, noninvasive measurement of the optical parameters of the phantom. The accuracy demonstrated provides the detectability of a few percent change in oxygenation of tissue blood. A simple method of analyzing the PRM data was developed based on the waveform moment analysis. Test of this method using a phantom demonstrated a very high sensitivity of the first moment to the phantom absorption coefficient. The differential measurement using two NIR wavelengths clearly demonstrates the utility for absolute qunatification of the oxygenation in addition to the total hemoglobin measurement. The breadboard sensor was further applied to verify the deep penetration capability of the PRM measurement, by measuring the depth information of a strongly absorbing layer in a dense scattering medium. A remarkable depth resolution of the breadboard sensor was demonstrated in this experiment suggesting the direct applicability of PRM/RET sensor for clinical deep tissue diagnosis.

Based on the preliminary results obtained up to date, we summarize the novel features and distinctive performance characteristics of the PRM/RET sensor below:

- Verification of PRM/RET technique - The feasibility experiment demonstrated a 100 fold improvement of the temporal resolution using PRM/RET technique over the conventional limit of the PRM technique, providing 40 psec resolution with a 200 MHz PRM system. This resolution was directly applied for the accurate temporal measurement of the deep tissue phantom response function allowing a high accuracy measurement of the phantom optical parameters.

- Quantitative measurement of tissue optical parameters - The breadboard system and simple analysis algorithm demonstrates a measurement accuracy of 0.001 cm^{-1} for absorption coefficient, μ_a, and 0.07 cm^{-1} for scattering coefficient, μ_s, of a homogeneous phantom closely resembling the soft tissue. This measurement accuracy is equivalent to a detectability of 1-2% variation of hemoglobin oxygenation, which is far better than any published results of non-invasive measurements. With an anticipated performance improvement of the prototype sensor, better than 1% accuracy will be obtained.

- Simultaneous differential measurement using common signal path - The unique orthogonal property of the PRM codes with different lengths allows a simultaneous differential measurement for multiple wavelengths using the common signal path from the transmitter optics to the digitizer. The differential measurement using two NIR wavelengths will provide the capability for accurate quantification of the hemoglobin oxygenation and total concentration in deep tissues.

- Large penetration depth with a high S/N - The breadboard system demonstrates penetration depth of over 8 cm in soft tissue with a S/N ratio of >20. Based on the design features, the next prototype will provide an even larger penetration depth with higher S/N ratio, with 1 second signal averaging. Neither the phase modulation spectroscopy (PMS) [Sevick et al, 1991] nor a conventional TRS system provides this level of sensitivity in an economic manner.

- Detection and localization of heterogeneity - Detection of strong absorption layer resembling heterogeneous blood concentration was demonstrated clearly in a simulation experiment using the breadboard system. The location of the layer was distinguished up to an 8 cm depth into the scattering medium resembling the soft tissue. Further improvement in resolution and penetration depth is expected with the prototype system.

- Compatibility with other diagnostic instrument for simultaneous operation - The unique noise and bias filtering capability will allow the sensor to operate in a noisy (both for optical and electrical) environment. Remote accessibility using fiber optics enables real time applications in surgical operations or other diagnostic processes.

- Continuous measurement with higher than 1 Hz updating rate - The unique signal processing technique of PRM/RET provides a high throughput signal with low transmitter power and allows a high data acquisition rate of over 1 Hz in the baseline configuration.

- Robust performance of a cost effective portable sensor package - A turnkey system continuously operational over a long period (more than several years) without maintenance requirements will be characteristic of the fully developed clinical system. The cost of the system is anticipated at no more than $20K. This system will be portable with less than 10 liter volume and lower than 50 Watt power consumption. No other TRS instrument offers such a benefit.

References

Buchweitz-Milton E. Weiss HR , Effect of MCA occlusion on brain O2 supply and consumption determined microspectrophotometrically, American Journal of Physiology. 253:H454-60, 1987.

Bulkley GB. Oshima A. Bailey RW., Pathophysiology of hepatic ischemia in cardiogenic shock, American Journal of Surgery, 151:87-97, 1986 .

Chance B. Leigh JS. Miyake H. Smith DS. Nioka S. Greenfeld R. Finander M. Kaufmann K. Levy W. Young M. et al., Comparison of time-resolved and -unresolved measurements of deoxyhemoglobin in brain, Proceedings of the National Academy of Sciences of the United States of America. 85:4971-5, 1988.

Chou CC, Splanchnic and overall cardiovascular hemodynamics during eating and digestion, Federation Proceedings, 42:1658-61, 1983 .

Duncan, A., T.L. Whitlock, M. Cope & D.T. Delpy, "A multiwavelength, wideband, intensity modulated optical spectrometer for near infrared and imaging," SPIE 1888:248-257, 1993.

Ferrari M. Hanley DF. Wilson DA. Traystman RJ, Redox changes in cat brain cytochrome-c oxidase after blood-fluorocarbon exchange, American Journal of Physiology. 258:H1706-13, 1990.

Ferrari M. Wilson DA. Hanley DF. Hartmann JF. Rogers MC. Traystman RJ, Non-invasive determination of hemoglobin saturation in dogs by derivative near-infrared spectroscopy, American Journal of Physiology, 256:H1493-9, 1989.

Ferrari M, Wilson DA, Hanley DF, Traystman RJ: Effects of graded hypotension on cerebral blood flow, blood volume and mean transit time in the dog. American Journal of Physiology, 262:H1908-14, 1992.

Flynn WJ Jr. Hoover EL., Allopurinol plus standard resuscitation preserves hepatic blood flow and function following hemorrhagic shock, Journal of Trauma. 37:956-61, Dec.1994.

Goldstein, A: Biostatistics: an introductory text. Macmillian, NY, p144, 1964.

Gopinath SP. Robertson CS. Grossman RG. Chance B., Near-infrared spectroscopic localization of intracranial hematomas, Journal of Neurosurgery, 79:43-7, 1993 .

Haida M and Chance B, Adv Exp Med Biol 345:829-35, 1994.

Hielscher AH, Tittel FK, and Jacques SL: Non-invasive monitoring of blood oxygenation by phase resolved transmission spectroscopy. SPIE 1888:275-88, 1993.

Jensen A. Hohmann M. Kunzel W., Redistribution of fetal circulation during repeated asphyxia in sheep: effects on skin blood flow, transcutaneous PO2, and plasma catecholamines, Journal of Developmental Physiology, 9:41-55, 1987 .

Lee, H.S. and N.T. Oneil, "Lidar return pulse profile and its relationship to water optical parameters," Proc. SPIE Ocean Optics VII, Monterey, CA, pp489-497, 1984.

Mancini DM. Bolinger L. Li H. Kendrick K. Chance B. Wilson JR, Validation of near-infrared spectroscopy in humans, Journal of Applied Physiology, 77:2740-7, 1994.

Nowicki PT. Stonestreet BS. Hansen NB. Yao AC. Oh W., Gastrointestinal blood flow and oxygen consumption in awake newborn piglets: effect of feeding, American Journal of Physiology, 245:G697-702, 1983.

Patterson, M. S., B. Chance, and W.C. Wilson, "Time resolved reflectance and transmittance for the noninvasive measurement of tissue optical properties," Appl. Opyic, Vol.28(12), pp2331-2336, 1989.

Seiyama A, Hazeki O, and Tamura M: Noninvasive quantitative analysis of blood oxygenation in rat skeletal muscle. J Biochem 103:419-424, 1988.

Sevick, E.M., J. Weng, M.B. Maris, B. Chance, "Analysis of absorption, scattering and hemoglobin saturation using phase-modulation spectroscopy," SPIE Vol. 1431, Time-resolved spectroscopy and imaging of tissues, 1991.

Tamura M, Oshino N, Chance B, Silver IA: Optical measurements of intracellular oxygen concentration of rat heart in vitro. Arch Biochem Biophysics 191:8-22, 1978.

van Assendelft OW: Spectrophotometry of Haemoglobin Derivatives., Charles C. Thomas, p55, 1970.

Villringer A. Planck J. Stodieck S. Botzel K. Schleinkofer L. Dirnagl U. Noninvasive assessment of cerebral hemodynamics and tissue oxygenation during activation of brain cell function in human adults using near infrared spectroscopy, Advances in Experimental Medicine & Biology, 345:559-65, 1994.

Wilson JR, Mancini DM, McCully K, Ferraro N, Lanoce V, and Chance B: Noninvasive detection of skeletal muscle underperfusion with near-infrared spectroscopy in patients with heart failure. Circulation 80:1668-1674, 1989.

Whipple GH: The hemoglobin of striated muscle. Am J Physiol 76:693-707, 1926.

Whitburn KD: The interaction of oxymyoglobin with hydrogen peroxide: The formation of ferryl myoglobin at moderate excesses of hydrogen peroxide. Arch Biochem Biophysics 253:419-430, 1987.

Wolfe WL and Zissis GJ, The Infrared Handbook, prepared by The Infrared Information and Analysis Center, Enviromental Research Institute of Michigan, 1978.

Wyatt JS. Cope M. Delpy DT. van der Zee P. Arridge S. Edwards AD. Reynolds EO, Measurement of optical path length for cerebral near-infrared spectroscopy in newborn infants, Developmental Neuroscience. 12:140-4, 1990.

Yarborough, JM, Taking the confusion out of matching medical lasers to applications. Photonics Spectra, pp88-94, Oct. 1992.

Appendix A. PRM Clock Circuit Diagram

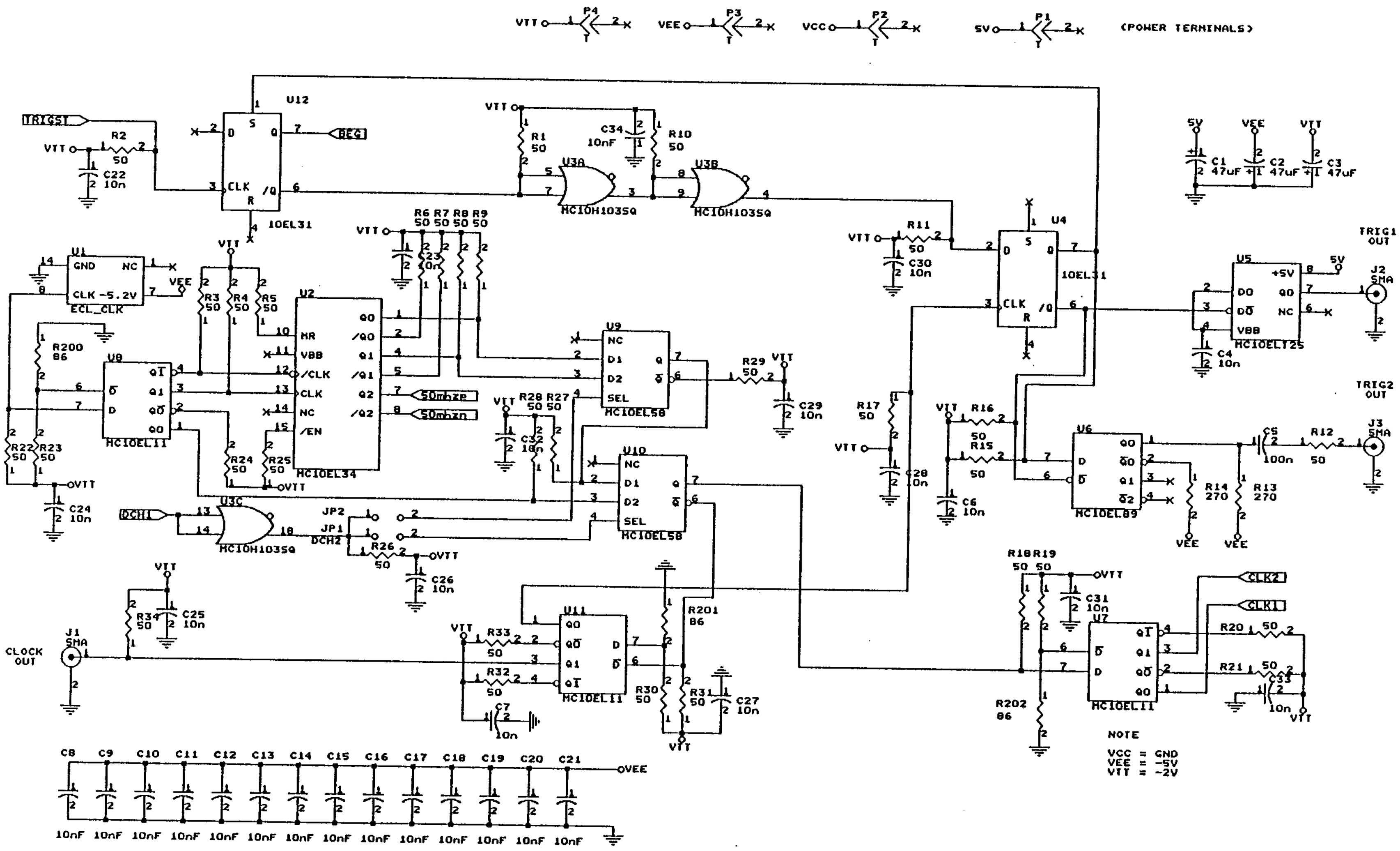

NOTE

VCC = GND
VEE = -5V
VTT = -2V

Science & Engineering Services, Inc.
4014 Blackburn Lane
Burtonsville, MD 20866

Title
Modified High Speed PN Code Generator

Size	Document Number	RE
B		2.

Date: September 8, 1995 Sheet 2 of

Appendix B. PRM Trigger Circuit Diagram

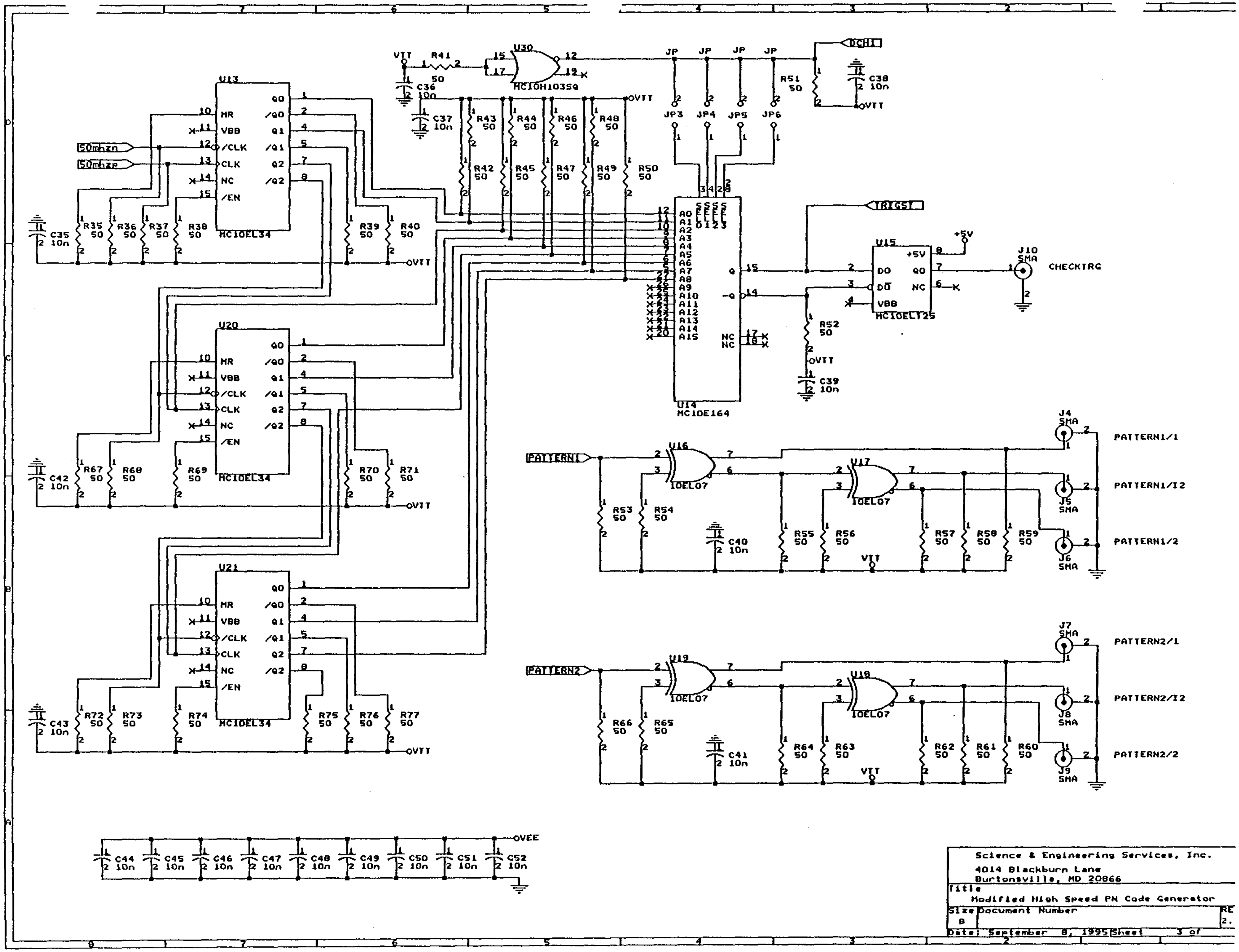

Science & Engineering Services, Inc.
4014 Blackburn Lane
Burtonsville, MD 20866

Title
Modified High Speed PN Code Generator

Size	Document Number	RE
B		2.

Date: September 8, 1995 Sheet 3 of

Appendix C. PRM Generator Circuit Diagram

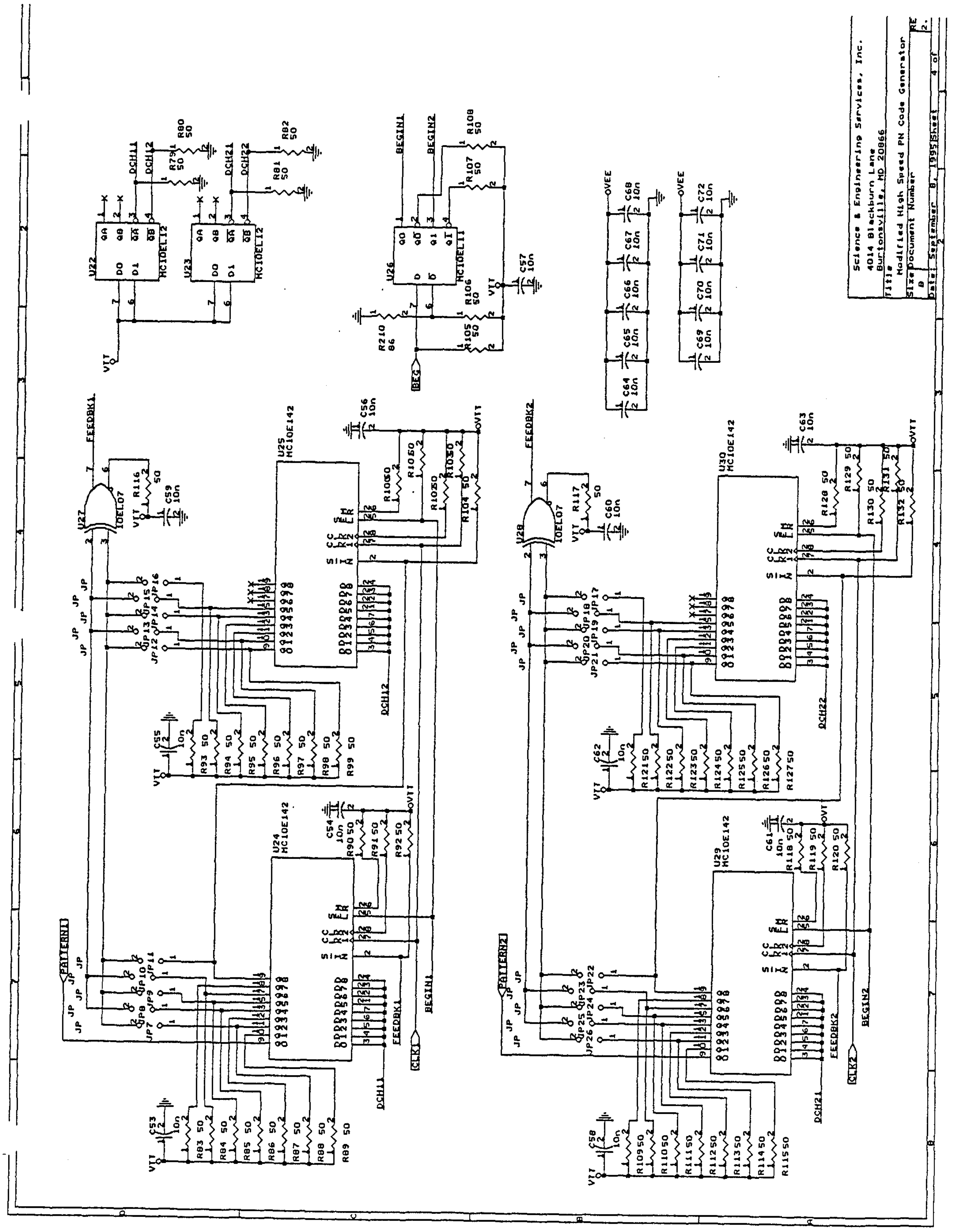

Science & Engineering Services, Inc.
4014 Blackburn Lane
Burtonsville, MD 20866

Title
Modified High Speed PN Code Generator

Size	Document Number	RE
B		2.

Date: September 8, 1995 Sheet 4 of

Received 2/8/2000

DEPARTMENT OF DEFENSE
UNITED STATES OF AMERICA

DEPARTMENT OF THE ARMY
US ARMY MEDICAL RESEARCH AND MATERIEL COMMAND
504 SCOTT STREET
FORT DETRICK, MARYLAND 21702-5012

REPLY TO
ATTENTION OF:

MCMR-RMI-S (70-1y) 21 Jan 00

MEMORANDUM FOR Administrator, Defense Technical Information
Center, ATTN: DTIC-OCA, 8725 John J. Kingman
Road, Fort Belvoir, VA 22060-6218

SUBJECT: Request Change in Distribution Statement

1. The U.S. Army Medical Research and Materiel Command has reexamined the need for the limitation assigned to technical reports written for the attached Awards. Request the limited distribution statements for Accession Document Numbers listed be changed to "Approved for public release; distribution unlimited." These reports should be released to the National Technical Information Service.

2. Point of contact for this request is Ms. Virginia Miller at DSN 343-7327 or by email at virginia.miller@det.amedd.army.mil.

FOR THE COMMANDER:

Phylis Rinehart

PHYLIS M. RINEHART
Deputy Chief of Staff for
Information Management

Encl
as